SAND REPORT

SAND 2003-0399
Unlimited Release
Printed February 2003

On Developing a Multifidelity Modeling Algorithm for System-Level Engineering Analysis

David R. Gardner and Gary L. Hennigan

Prepared by
Sandia National Laboratories
Albuquerque, New Mexico 87185 and Livermore, California 94550

Sandia is a multiprogram laboratory operated by Sandia Corporation,
a Lockheed Martin Company, for the United States Department of Energy's
National Nuclear Security Administration under Contract DE-AC04-94-AL85000.

Approved for public release; further dissemination unlimited.

Issued by Sandia National Laboratories, operated for the United States Department of Energy by Sandia Corporation.

NOTICE: This report was prepared as an account of work sponsored by an agency of the United States Government. Neither the United States Government, nor any agency thereof, nor any of their employees, nor any of their contractors, subcontractors, or their employees, make any warranty, express or implied, or assume any legal liability or responsibility for the accuracy, completeness, or usefulness of any information, apparatus, product, or process disclosed, or represent that its use would not infringe privately owned rights. Reference herein to any specific commercial product, process, or service by trade name, trademark, manufacturer, or otherwise, does not necessarily constitute or imply its endorsement, recommendation, or favoring by the United States Government, any agency thereof, or any of their contractors or subcontractors. The views and opinions expressed herein do not necessarily state or reflect those of the United States Government, any agency thereof, or any of their contractors.

Printed in the United States of America. This report has been reproduced directly from the best available copy.

Available to DOE and DOE contractors from
U.S. Department of Energy
Office of Scientific and Technical Information
P.O. Box 62
Oak Ridge, TN 37831

Telephone: (865) 576-8401
Facsimile: (865) 576-5728
E-Mail: reports@adonis.osti.gov
Online ordering: http://www.doe.gov/bridge

Available to the public from
U.S. Department of Commerce
National Technical Information Service
5285 Port Royal Rd
Springfield, VA 22161

Telephone: (800) 553-6847
Facsimile: (703) 605-6900
E-Mail: orders@ntis.fedworld.gov
Online ordering: http://www.ntis.gov/help/ordermethods.asp?loc=7-4-0#online

SAND 2003-0399
Unlimited Release
Printed February 2003

On Developing a Multifidelity Modeling Algorithm for System-Level Engineering Analysis

David R. Gardner and Gary L. Hennigan
Computational Sciences Department
Sandia National Laboratories
P. O. Box 5800, MS 0316
Albuquerque, NM 87185-0316

Abstract

Multifidelity modeling, in which one component of a system is modeled at a significantly different level of fidelity than another, has several potential advantages. For example, a higher-fidelity component model can be evaluated in the context of a lower-fidelity full system model that provides more realistic boundary conditions and yet can be executed quickly enough for rapid design changes or design optimization. Developing such multifidelity models presents challenges in several areas, including coupling models with differing spatial dimensionalities. In this report we describe a multifidelity algorithm for thermal radiation problems in which a three-dimensional, finite-element model of a system component is embedded in a system of zero-dimensional (lumped-parameter) components. We tested the algorithm on a prototype system with three problems: heating to a constant temperature, cooling to a constant temperature, and a simulated fire environment. The prototype system consisted of an aeroshell enclosing three components, one of which was represented by a three-dimensional finite-element model. We tested two versions of the algorithm; one used the surface-average temperature of the three dimensional component to couple it to the system model, and the other used the volume-average temperature. Using the surface-average temperature provided somewhat better temperature predictions than using the volume-average temperature. Our results illustrate the difficulty in specifying consistency for multifidelity models. In particular, we show that two models may be consistent for one application but not for another. While the temperatures predicted by the multifidelity model were not as accurate as those predicted by a full three-dimensional model,

our results show that a multifidelity system model can potentially execute much faster than a full three-dimensional finite-element model for thermal radiation problems with sufficient accuracy for some applications, while still predicting internal temperatures for the higher fidelity component. These results indicate that optimization studies with mixed-fidelity models are feasible when they may not be feasible with three-dimensional system models, if the concomitant loss in accuracy is within acceptable bounds.

Acknowledgments

We thank Joseph P. Castro, Jr. and Mark A. Gonzales for reviewing this report.

This work was supported by the Laboratory Directed Research and Development (LDRD) program at Sandia National Laboratories.

Contents

Figures

Tables

On Developing a Multifidelity Modeling Algorithm for System-Level Engineering Analysis

1 Introduction

In fulfillment of the national security mission of Sandia National Laboratories, engineers there simulate or test a wide variety of complex systems. These systems range from national infrastructure to nuclear power plants to weapons to micro-electrical-mechanical systems (MEMS) to living cells.

Historically, engineers at Sandia have relied on tests to characterize many such systems. Political, economic, and environmental factors increasingly constrain the ability of engineers to conduct tests as they have in the past. Sandia engineers must now rely increasingly on modeling and simulation of these disparate complex systems.

These disparate, complex systems must be modeled at many different levels of fidelity. For example, risk assessment studies for nuclear reactors are conducted with fault tree models in which the component models are of very low fidelity (*e.g.*, binary decisions) [1]. In contrast, studies of systems such as neutron generators use the highest fidelity physics models available, and tax the capabilities of the most powerful computers in the world [2].

As engineers rely more and more on modeling and simulation, they will also use more mixed-fidelity system simulations, simulations that contain models of differing fidelities. For example, a drift-diffusion model of a transistor might be used in a lumped-parameter circuit model to more accurately model the transistor behavior in a radiation environment [3].

In this report we discuss issues involved in multifidelity modeling and describe progress in developing an algorithm for multifidelity modeling for thermal radiation problems. This work is in support of the development of the *Entero* system simulation code package [4, 5]. The *Entero* code package is being developed for system-level analysis of entire nuclear weapons through the stockpile-to-target sequence. This is an ambitious, long-term goal.

A key design feature for the *Entero* code package is to allow the user to independently specify the level of fidelity for each module in the system [4, 5, 6, 7]. This feature allows users to put higher fidelity models in the modules of interest, while using models of lower fidelity in the other modules.

In the next section we review some previous work toward developing multifidelity models. Then we discuss issues involved in multifidelity modeling. Next we describe progress toward developing an algorithm for multifidelity modeling for thermal radiation problems. Finally we present some conclusions and recommendations for future research.

2 Overview of Multifidelity Modeling Concepts

As engineers rely more and more on modeling and simulation, they will also use more multifidelity simulations. In this report we use the term *multifidelity model* to mean a model in which the fidelity of the components of the model for a system can be changed. Thus at least one component in the system model can be represented by at least two component models, each with a different fidelity. For example, a transistor in an electrical circuit might be represented by either a (zero-dimensional) behavioral model or by a (one-, two- or three-dimensional) drift-diffusion model. Sometimes an analyst analyzes the system using one model or the other for the transistor.

To emphasize cases where the fidelities of the component models used in a system model are different—for example, a drift-diffusion model of a transistor embedded in a model in which all the other components are represented by behavioral models—we will sometimes use the term *mixed-fidelity* model or simulation.

Such mixed-fidelity models have several advantages. They enable a component design to be evaluated in the context of a full system, and allow more realistic boundary conditions for the model of the component. They enable more rapid system-level analysis and optimization, because changes to the higher fidelity model can be incorporated directly into the system model without constructing an equivalent lower fidelity model. They enable the uncertainty in knowledge of a component to be reflected in the fidelity of the model used for the component, independent of the fidelities of models used for other components. And the resolution and fidelity of the simulation can be tailored to the requirements of the analysis, using lower fidelity models for exploratory studies and hence making better use of computing and personnel resources [8, 9].

2.1 Multiresolution Combat Modeling

Much of the exploration of mixed-fidelity modeling has been carried out in the context of combat modeling [10]. In this context, *variable-resolution* models are models or families of models in which users can change the resolution at which phenomena are treated [11, 12, 13, 14, 15], and *cross-resolution* modeling is linking models with different resolutions [11, 12, 14, 16, 17].

In combat modeling, a model with higher resolution has more components or more details than one with lower resolution. For example, a lower resolution model of a battalion of tanks might describe the battalion as a whole by the number of tanks and some average location of the battalion, while a higher resolution model might describe the motions of the individual tanks.

Davis and Bigelow note that *resolution* is often defined simply as "the level of detail at which system components and their behaviors are depicted" [10]. In the context of combat modeling, this definition for resolution is ambiguous because it can be applied to many different features of the model, including the spatial scale, the temporal scale, the physical processes included, the number of objects, the number of attributes of each object, and the degree of interaction between objects.

One objective for combat modeling is to develop the ability to use *multiresolution* models. *Multiresolution modeling* is building a single model or a family of models with alternative user modes involving different levels of resolution for the same phenomena [18, 10, 19].

In multiresolution combat modeling, lower resolution entities must interact with entities with higher resolution. When a higher resolution entity must interact with a lower level entity, one model or the other must be changed so that they can interact at the same level of resolution. For example, consider a single tank (a higher resolution entity) interacting with a battalion of tanks treated as a single entity (a lower resolution entity). The process of dynamically changing model resolution is called *disaggregation* if the resolution of the model for the lower resolution entity is increased in resolution to correspond to the resolution of the model for the higher resolution entity. The process of dynamically changing model resolution is called *aggregation* if the resolution of the model for the higher resolution entity is decreased in resolution to correspond to the resolution of the model for the lower resolution entity. The problem of linking simulations at different resolutions is called the aggregation-disaggregation problem [16, 17, 19, 20, 21, 22, 23].

The process of creating a lower resolution model from a higher resolution one is called *model abstraction* [8, 19, 24, 25, 26, 27, 28, 29, 30]. Model abstraction is an active area of research.

2.2 Model Consistency

A much-discussed issue in multiresolution modeling is whether a lower resolution model and a higher level model are *consistent*. A lower resolution model and a higher resolution model are said to be *weakly consistent* if the projection of the state of the higher resolution model to the space of the lower resolution model is sufficiently close to the state of the lower resolution model. For example, a three-dimensional thermal model might be weakly consistent with a zero-dimensional thermal model if the average temperature of the three-dimensional model is within a specified tolerance of the temperature of the zero-dimensional model.

A lower resolution model and a higher resolution model are said to be *strongly consistent* if the projection of the state of the lower resolution model to the space of the higher res-

olution model is sufficiently close to the state of the higher resolution model. For example, a zero-dimensional thermal model might be strongly consistent with a three-dimensional thermal model if the single temperature of the zero-dimensional model when projected to the space of the three-dimensional model is within a specified tolerance of the temperature field of the three-dimensional model.

Strong consistency thus defined is much rarer than weak consistency. Whether the model states are "sufficiently close" depends on the modeling perspective. For example, it may be sufficient for a graph generated from the lower resolution model to indicate the same trends as a graph generated from the projected state of the higher resolution model [10, 31].

This view of model consistency however assumes that the higher resolution model is more accurate than a corresponding lower resolution model. However, the addition of more detail does not necessarily improve the accuracy of a model [10, 24]. And in practice, lower resolution models are used frequently and successfully. For example, many engineering systems such as bridges and automobiles are designed and built using classical mechanics rather than relativistic mechanics, even though the latter is more accurate.

Despite the deficiencies of the definitions of weak and strong consistency, we will apply these definitions in discussing the models described later in this report (Section 5).

2.3 Numerical Zooming

The term *numerical zooming* has also been used to describe simulations in which one component of the system has a higher fidelity than the others, *i.e.*, mixed-fidelity modeling. For example, Reed and Afjeh used a three-dimensional, Navier-Stokes model of a fan to compute performance maps for zero-dimensional thermodynamic component models in a turbofan engine simulation [32, 33, 34]. Follen and auBouchon have implemented mixed-fidelity modeling in the National Cycle Program of the National Propulsion System Simulation by inserting one-dimensional compressor models in a zero-dimensional model of a turbofan engine [9].

3 Issues in Multifidelity Modeling

A variety of issues arise in multifidelity modeling. These include integrating models with differing dimensionalities (*e.g.*, integrating a zero-dimensional thermal model with a three-dimensional, finite-element thermal model), integrating models with differing spatial resolutions, integrating physics with differing time scales, integrating models with differing time scales, and verification and validation of multifidelity models.

3.1 Integrating Models with Differing Spatial Dimensionalities

Integrating models with differing spatial dimensionalities, which is the focus of this work, presents significant difficulties in determining the appropriate method of projection to use from the lower dimensional model to the higher dimensional model and from the higher dimensional model to the lower dimensional model. Various types of averages may be used to project the higher dimensional variable field to the lower dimensional one. For example, a three-dimensional temperature field represented by nodal values on a finite-element mesh can be projected to a zero-dimensional model using a surface or volume average of the temperature (we explore the use of both average temperatures in this work). To project a zero-dimensional temperature to a three-dimensional temperature field on a finite-element mesh requires applying the single temperature to the boundary of the three-dimensional mesh, or a portion of the boundary. Such projections produce unknown errors in the resulting solutions.

3.2 Integrating Models with Differing Spatial Resolutions

Integrating models with different spatial resolutions presents significant difficulties. For example, abrupt changes in mesh resolution in shock-wave physics simulations can result in non-physical reflections when waves traverse a region of changing mesh [35, p. 237]. Variable meshes can also result in increased error in the solution, rather than decreased error [35, pp. 288–290]. In addition, for explicit codes, the time step for the integrated models is controlled by the Courant-Friedrichs-Levy limit for the smallest mesh cell. Thus variable spatial resolution may reduce the required computer memory (because fewer cells are used), but it may not reduce the simulation execution time. Therefore, care must be exercised in integrating models with different spatial resolution.

3.3 Integrating Physics with Differing Time Scales

Different physical phenomena are characterized by different time scales. For example, chemical reactions in a fluid flow frequently occur very rapidly compared to the time scale of the fluid flow. For the problems the *Entero* code package is designed to address, time scales may range from nanoseconds for nuclear reactions to years for aging effects. Numerical models with both a shorter time scale and a longer time scale are said to be stiff, because the numerical computation of the solution on the longer time scale is strongly affected by the presence of the shorter time-scale component. Integrating models with differing time scales must be performed carefully to ameliorate problems with stiffness.

3.4 Integrating Models with Differing Time Scales

Models of different fidelity may have differing time steps. These differences may be due to different physical time scales (Section 3.3) or may be due to different numerical techniques. For example, the time steps allowed for a model using an explicit time-integration scheme will be limited by the Courant-Friedrichs-Levy limit (Section 3.2). The time steps allowed for a model using an implicit time-integration scheme are not limited by the Courant-Friedrichs-Levy limit. If a model using an explicit time-integration scheme is integrated with a model using an implicit scheme, time steps in the latter model will be limited by the Courant-Friedrichs-Levy limit via the integration to the model with the explicit scheme[1]. For multifidelity models, the time step sizes must be coordinated, which imposes an additional constraint on the system model.

3.5 Consistency and Accuracy of Multifidelity Models

As discussed in the previous section, an important issue in multiresolution modeling is whether a higher resolution model and a lower level model are consistent. In practice, lower resolution models are used frequently and successfully. For example, we frequently use classical mechanics rather than quantum mechanics. See especially [8, 10, 19, 24].

A higher resolution model is often inferred to be more accurate than a lower resolution model. However, the addition of more detail does not necessarily improve accuracy [36, 24].

3.6 Verifying and Validating Multifidelity Models

Verifying and validating mixed-fidelity system models is a difficult problem. There are few analytic solutions for mixed-fidelity models, so that verifying the models may rely on verified higher-fidelity simulations. Mixed-fidelity experiments are difficult to perform, so validating mixed-fidelity models directly against experimental data is problematic. It may be that the only method for validating mixed-fidelity models is to validate them against verified and validated higher fidelity simulations.

[1]This limitation may be partially alleviated if the model with the explicit scheme can be advanced by multiple time steps before the model with the implicit scheme must be updated.

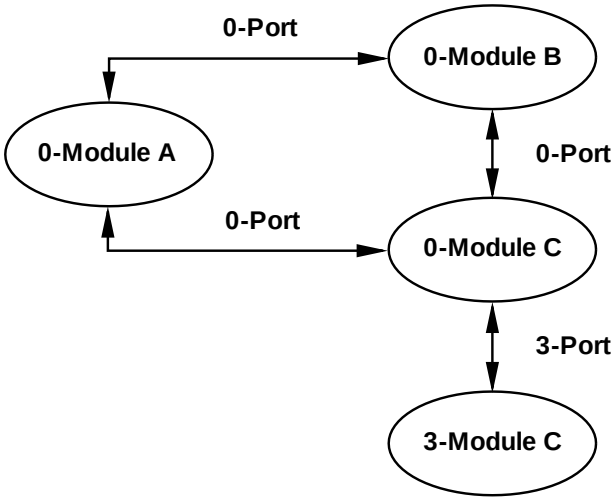

Figure 1. Illustration of Mixed-Fidelity System Models. Three zero-dimensional components are connected via 0-Ports into a system. Module C is represented by a higher fidelity component, namely, a three-dimensional component, that is connected to the zero-dimensional one via a 3-Port.

4 A Multifidelity Algorithm for Thermal Radiation

We now describe a multifidelity algorithm for thermal radiation. In the algorithm, a zero-dimensional model of the system controls a simulation. This model consists of a set of software objects that identify and manage the model or models used for physical phenomena in the actual component, and a set of objects that identify and manage the information exchange between the objects.

In the algorithm, a zero-dimensional model of the system controls a simulation. At the zero-dimensional level, the physical state of a component is represented by a set of scalar variables that represent an appropriate average for the component (*e.g.*, temperature or pressure). Physical connections between components are represented by information transfer through the interconnection objects, which are called *ports*. For example, consider a system consisting of two solid bodies exchanging energy by thermal radiation. Each body has an average temperature assigned to it. The port describing the interaction records the temperature of each body and indicates that the energy transfer is via thermal radiation.

The zero-dimensional model of a component may be augmented by an alternate model. This is done by connecting the zero-dimensional model to the alternate model with a special port, called an N-Port, that transforms information (Figure 1). For information transferred

from the zero-dimensional model to the alternate model, the N-Port transforms the zero-dimensional state variables to those used by the alternate model. For information transferred from the alternate model, the N-Port transforms the state variables from those used by the alternate model to the scalar state variables used by the zero-dimensional model. (The Port connection between zero-dimensional models is a special case of the N-Port, the 0-Port.)

As an example, consider a system of two components that are interacting via thermal radiation. The zero-dimensional temperature of each component is an average temperature. Suppose that the temperature of one of the components is modeled with a three-dimensional finite-element model. This model is connected to the zero-dimensional model for the component by an N-Port. For transferring information from the zero-dimensional model to the three-dimensional model, the N-Port maps the single temperature of the zero-dimensional model to a portion of the finite-element mesh surface visible to the zero-dimensional component. For transferring information from the three-dimensional model to the zero-dimensional model, the N-Port computes an average temperature (either a surface-averaged temperature or a volume-averaged temperature) from the three-dimensional model to send to the zero-dimensional model. (This resembles the approach used in the National Cycle Program [9].)

The algorithm consists of the following steps listed in Table 1. We describe the implementation of the algorithm in Appendices 7 and 8.

5 Tests of the Multifidelity Algorithm

We tested the algorithm on a system consisting of five modules: The environment, the case, the package, the arming, fuzing, and firing module (AF&F), and the safety device. The geometry for the test system is shown schematically in Figure 2. Geometric dimensions for the system and properties for the module materials are given in Appendix 1.

We compared predicted temperatures from three models of the test system: a full three-dimensional model (denoted the *3D* model) as the system baseline, a mixed-fidelity system model (denoted the *MD* model), and a zero-dimensional system model (denoted the *0D* model).

In the 0D model, each component was represented by a zero-dimensional model for temperature, that is, each component had a single temperature (Figure 3).

In the MD model, the AF&F was represented by a three-dimensional finite-element mesh. The mesh was composed of 1083 nodes and 852 hexahedral elements (Figure 4).

In the 3D model, each component was represented by a finite-element mesh (Figure 5). The package, AF&F, and safety device were represented by hexahedral meshes; the mesh

Table 1. The Mixed-Fidelity Algorithm

1. Identify the components in the system and their physical interconnections. This identifies the zero-dimensional model for the system.

2. Identify the alternate models to be used for system components.

3. Initialize state variables of the zero-dimensional models from the state variables of the alternate models or using specified values.

4. Increment the time variable and advance the state of zero-dimensional system model to the new time.

5. For the alternate models, transform the zero-dimensional state variable values to the values needed by the alternate models as boundary conditions.

6. Advance the state of the alternate model to the current time.

7. Transform the variables for the alternate model to the state variables needed by the zero-dimensional system model.

8. Repeat steps 4 through 7 until the final problem time has been reached.

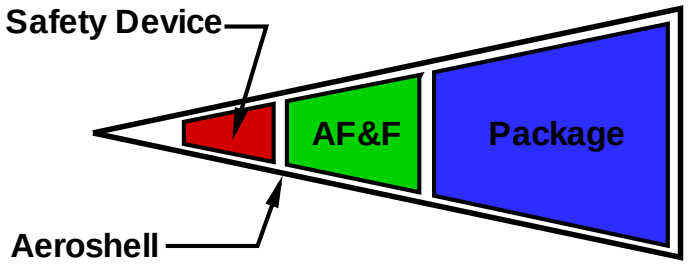

Figure 2. The Test System. The test system consists of four component modules plus the environment. The modules are not drawn to scale.

for the AF&F was the same mesh used in the mixed-fidelity model. Shell elements were used for the aeroshell. The three-dimensional system model had 8585 nodes and 7629 elements.

We used three test problems for assessing the performance of the algorithm: a heating problem, a cooling problem, and a problem with a time-dependent thermal radiation boundary condition.

We assessed the performance of the algorithm based on comparisons of surface-average temperatures, volume-average temperatures, minimum temperatures, maximum temperatures, and temperatures at selected special points (called thermal pins) inside the AF&F. In the terminology introduced in Section 2.2, we assessed the performance of the algorithm based on weak consistency: The trends in the surface-average temperatures, volume-average temperatures, minimum and maximum temperatures, and temperatures at selected internal points for the AF&F predicted by the MD model should match those in the 3D model and the values of the temperatures should be ”sufficiently close”, where what constitutes being ”sufficiently close” was deliberately not defined precisely. For practical purposes, if the maximum difference in temperature over the time of the simulation was less than 100 K, one could consider the temperatures to be ”sufficiently close” to assert that the models are weakly consistent.

In order to connect a zero-dimensional model to a three-dimensional finite-element model, the temperature field from the latter must be transformed to a single temperature. Two obvious candidates for this temperature are the surface-average temperature and the volume-average temperature. Based on energy conservation, one might expect the volume-average temperature to give reasonable results (Appendix 8). However, radiative heat transfer depends on surface temperatures, so one might also expect the surface-average temperature to give reasonable results. In this report we present results from using both the surface-average temperature and the volume-average temperature.

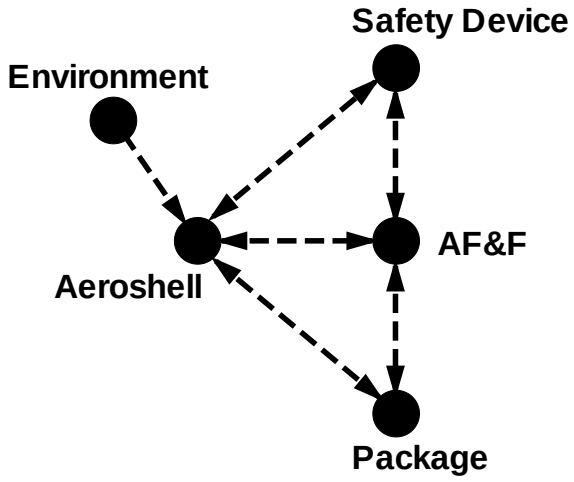

Figure 3. The Zero-Dimensional Test System (0D Model). The arrows indicate explicit information exchange.

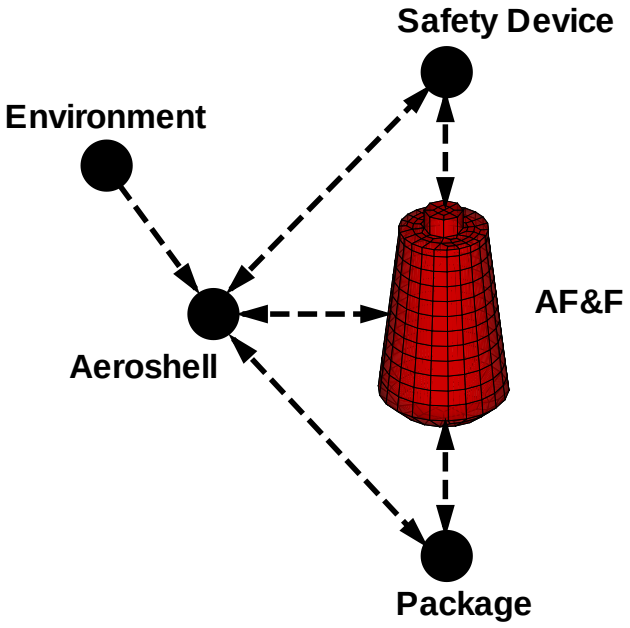

Figure 4. The Mixed-Fidelity Test System (MD Model). The arrows indicate explicit information exchange.

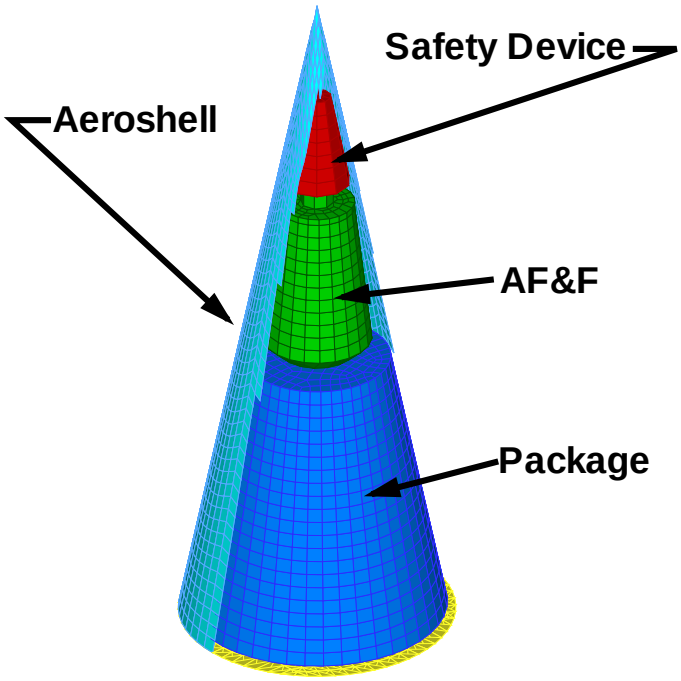

Figure 5. The Three-Dimensional Test System (3D Model).

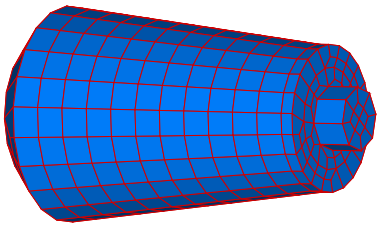

Figure 6. AF&F Mesh Used in the Mixed-Fidelity Model.

5.1 The Heating Problem

In the heating problem, the environment was a constant temperature of 1033 K with the system at an initial temperature of 300 K.

5.1.1 Heating Case 1: Exchanging the Surface-Average Temperature

Heating Case 1 is the case of the heating problem in which the surface-average temperature of the AF&F was exchanged with the zero-dimensional system model in the MD model.

Figure 7 shows the surface-average temperatures predicted for the AF&F by the three system models for Heating Case 1. Initially the surface-average temperatures in the AF&F in the 3D and MD models are essentially identical and increase more rapidly than the surface-average temperature of the AF&F in the 0D model. This is a consequence of the finite thermal conductivity in the AF&F. Note that the shell elements used in the 3D model allow conduction in the plane of the element but ignore conduction in the shell thickness [37], so for uniform external boundary conditions they behave like the zero-dimensional model for the aeroshell.

The temperature of the entire volume of the AF&F in the 0D model must increase uniformly, while in the 3D and MD models the thermal energy is initially confined near the surface of the AF&F by the finite thermal conductivity, resulting in higher surface-average temperatures early in the simulation. Because the package must also heat uniformly in the 0D model, it acts as a large thermal sink, further retarding the rate of temperature increase in the AF&F.

Given the discussion of model consistency and the results in Figure 7, the MD and 3D models are weakly consistent in terms of trends based on surface-average temperature. Depending on how "sufficiently close" is defined, the 0D and MD models may be weakly consistent in terms of the temperature values.

Although the surface-average temperature of the 0D model increases more slowly than the surface-average temperature of the 3D model, this results in a greater rate of heat transfer to the AF&F in the 0D model compared to the 3D model. The volume-average temperature of the AF&F in the 0D model in fact increases more rapidly than the volume-average temperature in the 3D model (Figure 8). These differences are due to the finite thermal conductivity in the AF&F in the 3D model.

From the data in Figure 8, the MD and 3D models are weakly consistent based on trends, but none of the models are consistent based on temperature values.

As in the 0D model, the rate of increase in the surface-average temperature of the AF&F in the MD model is decreased by the effect of the package module, which acts as a large thermal sink. This effect is visible in the temperature contours shown in Figure 9, which

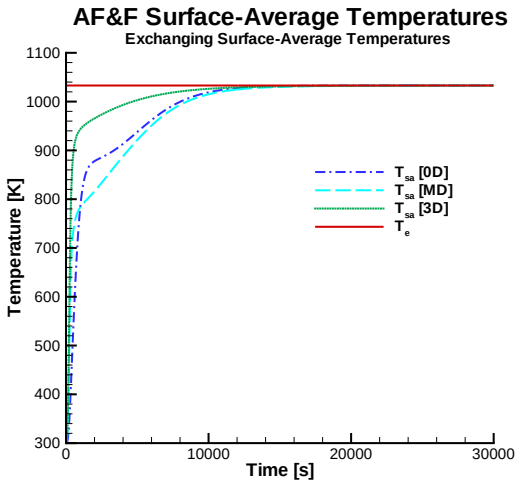

Figure 7. Surface-Average Temperatures in the AF&F for Heating Case 1 (Constant-Temperature Environment; Exchanging Surface-Average Temperature in the MD Model).

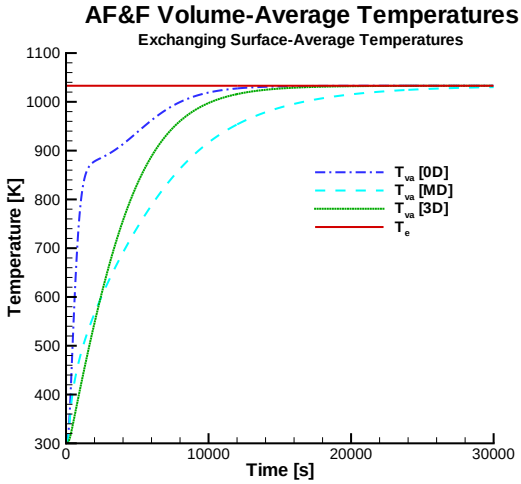

Figure 8. Volume-Average Temperatures for the AF&F for Heating Case 1 (Constant-Temperature Environment; Exchanging Surface-Average Temperature in the MD Model).

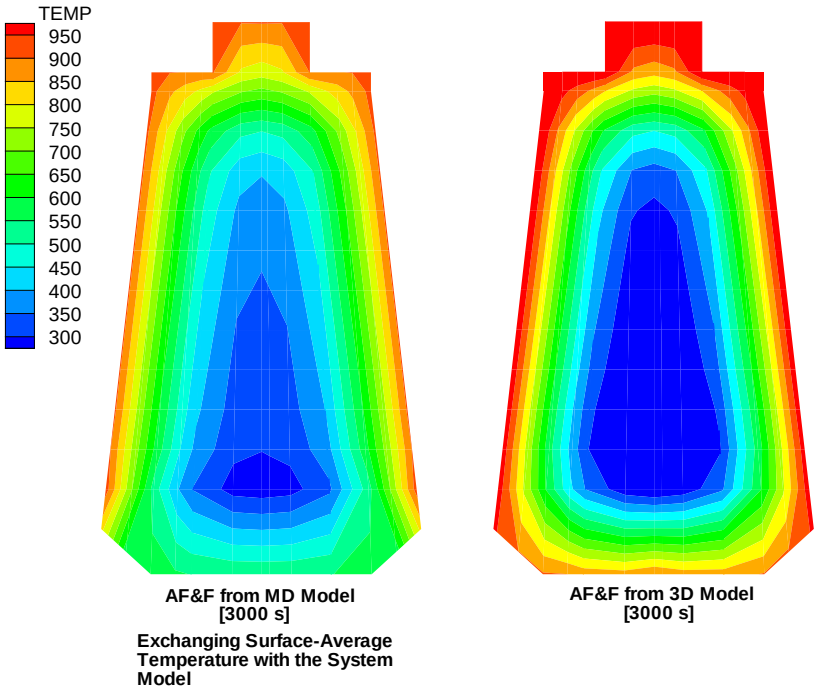

Figure 9. Comparison of Internal Temperatures for the AF&F— Predicted by the MD and 3D Models for Heating Case 1 (Exchanging Surface-Average Temperatures in the MD Model) at 3000 s. Left: The MD Model. Right: The 3D Model.

shows contours on a cross section containing the axis of the AF&F at 3000 seconds (a time when the difference between the surface-average temperatures of the MD and 3D models is large).

From the data in Figure 9, the MD and 3D models are weakly consistent based on trends, but inconsistent based on visual assessment of the locations of temperature values.

The volume-average temperature for the AF&F in the MD model increases more slowly than the volume-average temperatures for the AF&F in either the 0D or 3D models due to the finite thermal conductivity in the AF&F in the MD model (which slows the transfer of heat to the interior) and the influence of the package as a large thermal sink (so that there is a net thermal energy transfer from the AF&F to the package) (Figure 8).

We show the maximum and minimum temperatures in the AF&F for the MD and 3D system models in Figures 10 and 11, respectively. Except at very early times and later times, the maximum AF&F temperatures predicted by the MD and 3D models are signifi-

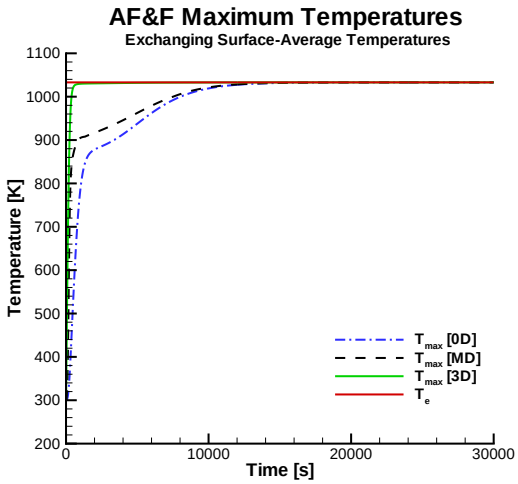

Figure 10. Maximum Temperature in the AF&F for Heating Case 1 (Exchanging Surface-Average Temperatures in the MD Model).

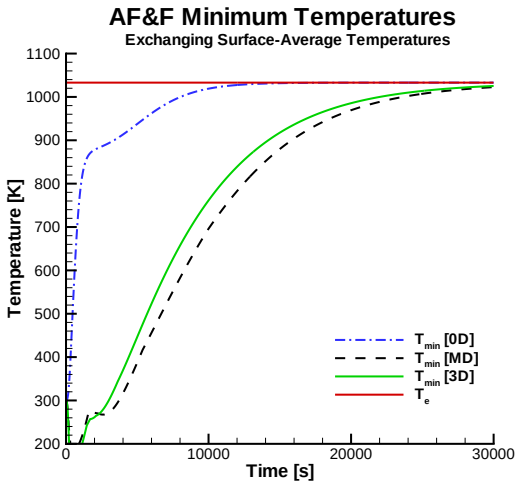

Figure 11. Minimum Temperature in the AF&F for Heating Case 1 (Exchanging Surface-Average Temperatures in the MD Model).

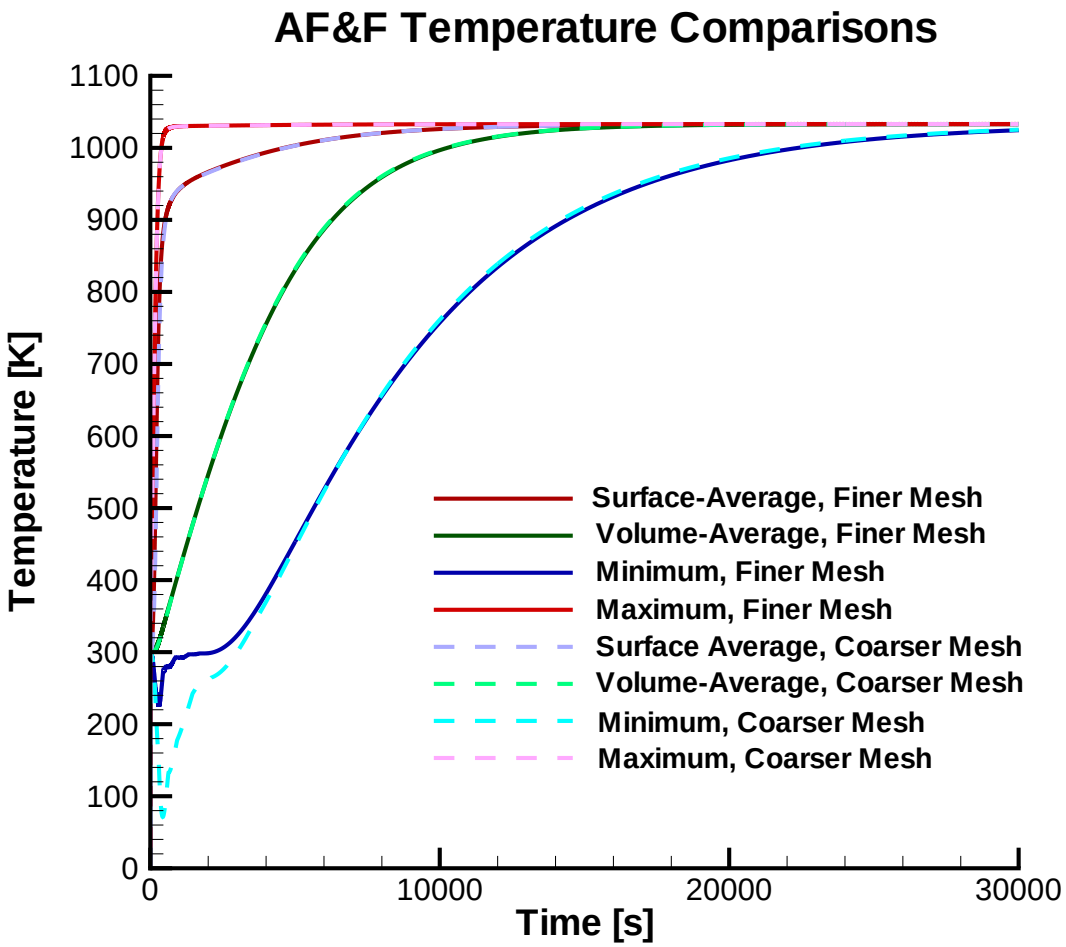

Figure 12. Comparison of Temperatures for the Normal Mesh and a Refined Mesh in the AF&F for Heating Case 1 (Exchanging Surface-Average Temperatures in the MD Model).

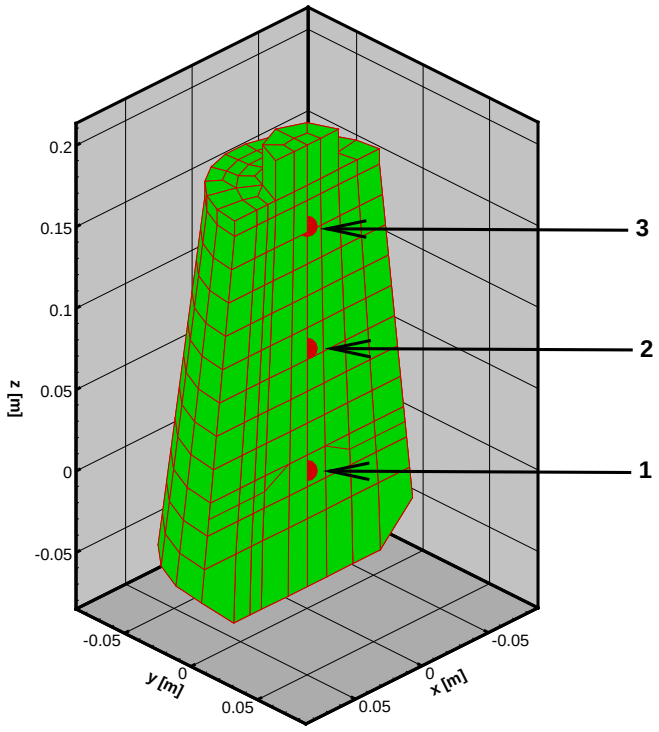

Figure 13. Locations of Thermal Pins in the AF&F.

cantly different (Figure 10). The maximum temperature of the AF&F in the MD model is lower than the maximum temperature in the AF&F in the 3D model because in the former model the package acts as a large thermal sink and moderates the maximum temperature. In contrast, the minimum temperatures follow similar trends and are reasonably close (Figure 11) because they are not significantly influenced by the thermal sink.

From the data in Figure 10, the MD and 3D models are weakly consistent based on trends, but inconsistent based on temperature values.

From the data in Figure 11, the MD and 3D models are weakly consistent based on trends and on temperature values.

The minimum temperatures below 300 K at early times in the simulations (Figure 11) are artifacts of the mesh resolution. To demonstrate this, we reran the three-dimensional simulation for Heating Case 1 using a mesh with 34916 hexahedral elements (5376 elements in the AF&F; the standard mesh had 852 hexahedral elements in the AF&F) and 13082 shell elements. Temperatures from the simulation with the refined mesh are plotted in Figure 12. The surface-average, volume-average, and maximum temperatures predicted by the simulations with the coarser and finer meshes are essentially identical. The physically unrealistic minimum temperatures below 300 K predicted at early times in the coarser mesh simulation are significantly improved in the simulation with the finer mesh models, and the temperatures predicted at later times (greater than approximately 2000 seconds) are essentially identical.

The temperature histories at three thermal pins distributed along the vertical axis of the AF&F (Figure 13) are shown in Figures 14–16. The temperatures predicted by the MD model at Thermal Pin 2 are close to those predicted by the 3D model at that pin (Figure 15). This is because near the center of the AF&F, the moderating thermal effect of the package in the MD model is diminished. However, the temperatures predicted by the MD model at Thermal Pin 1 are not good approximations to the temperatures predicted by the 3D model at that pin (Figure 14). And the temperatures predicted by the MD model at Thermal Pin 3 are not good approximations to the temperatures predicted by the 3D model at that pin. Temperatures at pins 1 and 3 are more strongly affected by the surrounding modules.

From the data in Figure 14, the MD and 3D models are weakly consistent based on trends, but inconsistent based on temperature values at Thermal Pin 1.

From the data in Figure 15, the MD and 3D models are weakly consistent based on trends and on temperature values at Thermal Pin 2.

From the data in Figure 16, the MD and 3D models are (perhaps) weakly consistent based on trends, but inconsistent based on temperature values at Thermal Pin 3.

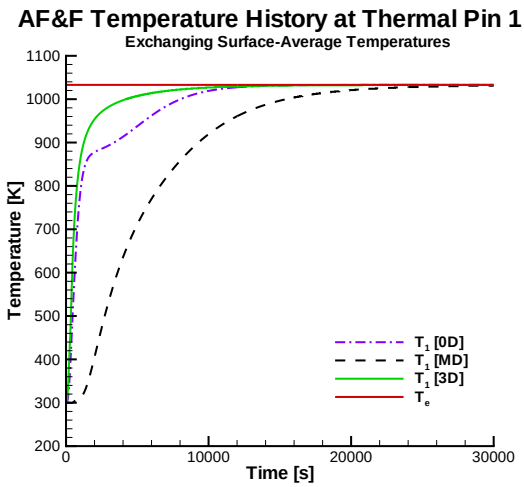

Figure 14. Temperature Histories for Thermal Pin 1 in the AF&F for Heating Case 1 (Exchanging Surface-Average Temperatures in the MD Model).

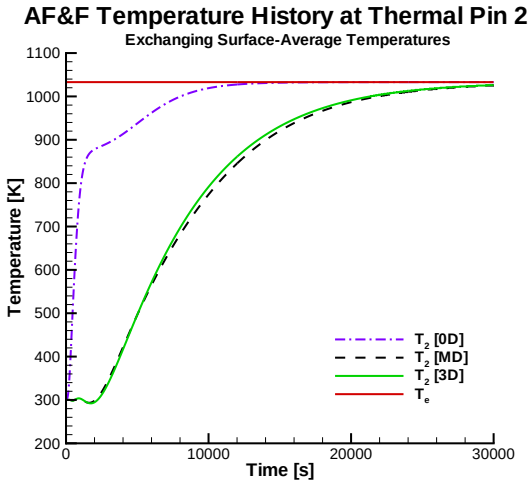

Figure 15. Temperature Histories for Thermal Pin 2 in the AF&F for Heating Case 1 (Exchanging Surface-Average Temperatures in the MD Model).

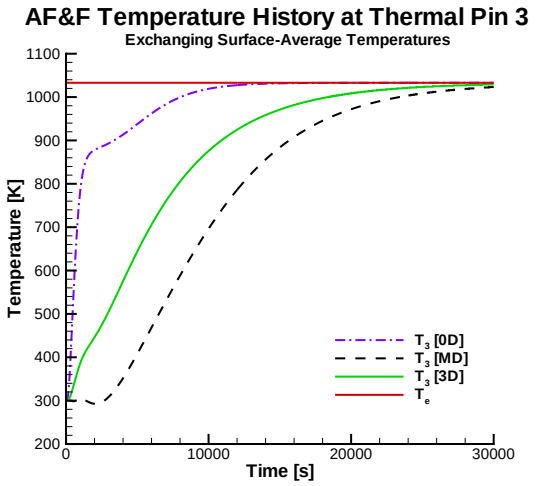

Figure 16. Temperature Histories for Thermal Pin 3 in the AF&F for Heating Case 1 (Exchanging Surface-Average Temperatures in the MD Model).

5.1.2 Heating Case 2: Exchanging the Volume-Average Temperature

Heating Case 2 is the case of the heating problem in which the volume-average temperature of the AF&F was exchanged with the zero-dimensional system model in the MD model.

Figure 17 shows the surface-average temperatures and Figure 18 shows the volume-average temperatures predicted for the AF&F by the three models for Heating Case 2. The results are similar for both the surface-average temperatures (compare Figures 7 and 17) and the volume-average temperatures (compare Figures 8 and 18). Because the volume-average temperature depends on the heating of the entire volume, it lags the surface-average temperature and so more time is required for the AF&F to reach the temperature of the environment.

The surface-average temperatures of the AF&F in the 3D and MD models (Figure 17) initially increase faster than the surface-average temperature of the AF&F in the 0D model due to the finite thermal conductivity in the former model. The temperature of the entire volume of the AF&F in the 0D model must increase uniformly, while in the 3D and MD models the thermal energy is initially confined near the surface of the AF&F by the finite thermal conductivity, resulting in higher surface-average temperatures.

Although the surface-average temperature of the 0D model increases more slowly than the surface-average temperature of the 3D model, this results in a greater rate of heat transfer to the AF&F in the 0D model compared to the 3D model. The volume-average temper-

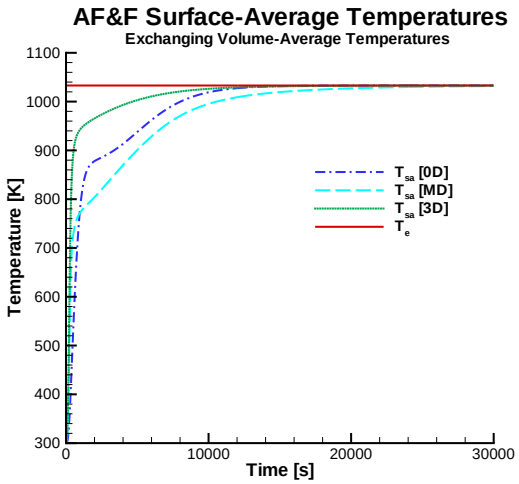

Figure 17. Surface-Average Temperatures for the AF&F in Heating Case 2 (Constant-Temperature Environment; Exchanging Volume-Average Temperature in the MD Model).

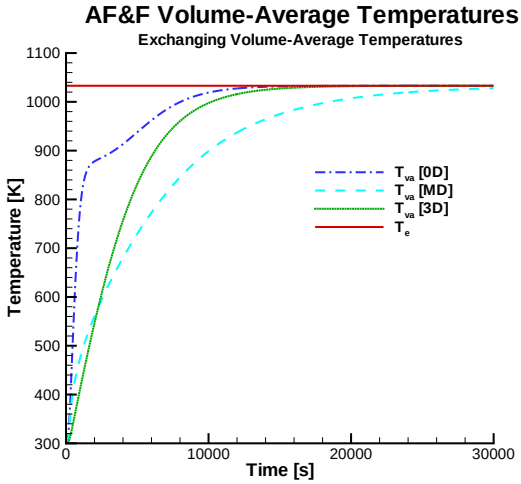

Figure 18. Volume-Average Temperatures for the AF&F in Heating Case 2 (Constant-Temperature Environment; Exchanging Volume-Average Temperature in the MD Model).

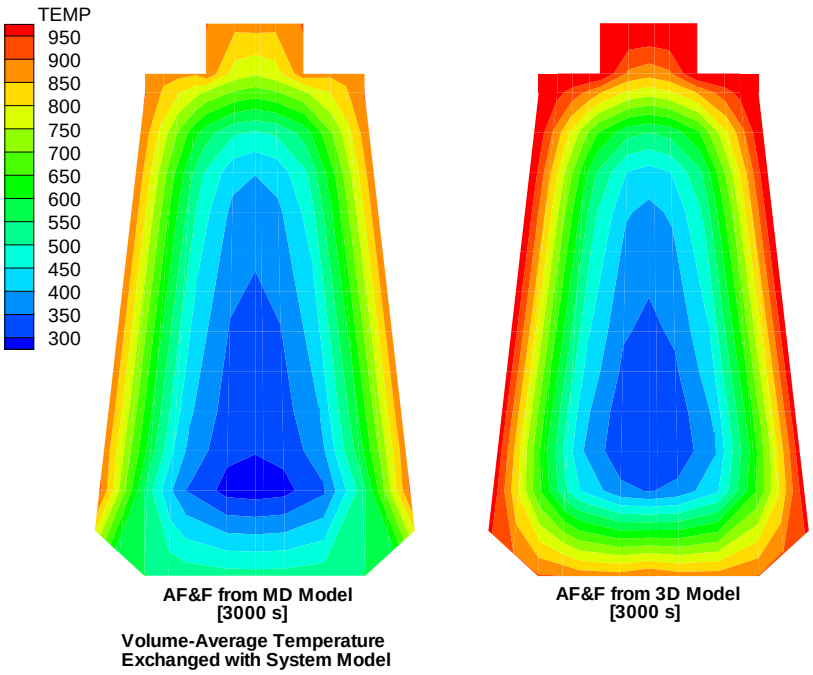

Figure 19. Comparison of Internal Temperatures for the AF&F— Predicted by the MD and 3D Models for Heating Case 2 (Exchanging Volume-Average Temperatures in the MD Model) at 3000 s. Left: The MD Model. Right: The 3D Model.

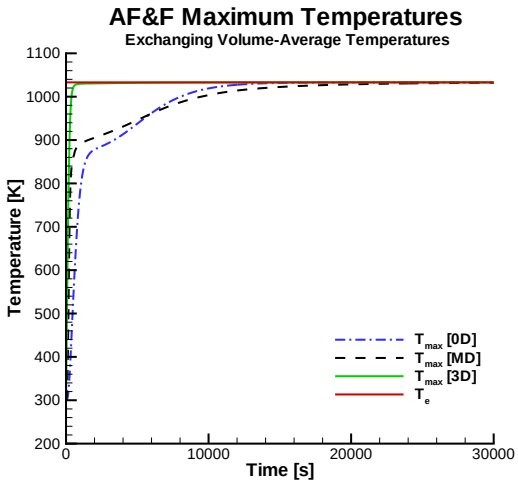

Figure 20. Maximum Temperature in the AF&F for Heating Case 2 (Exchanging Volume-Average Temperatures in the MD Model).

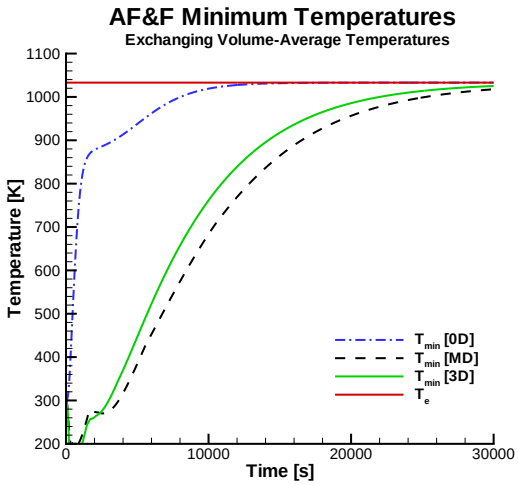

Figure 21. Minimum Temperature in the AF&F for Heating Case 2 (Exchanging Volume-Average Temperatures in the MD Model).

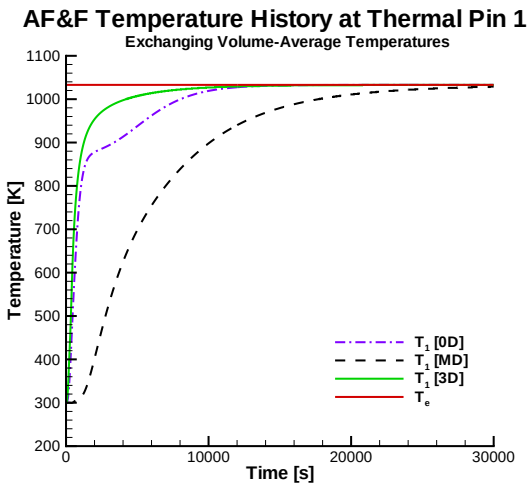

Figure 22. Temperature Histories for Thermal Pin 1 in the AF&F for Heating Case 2 (Exchanging Volume-Average Temperatures in the MD Model).

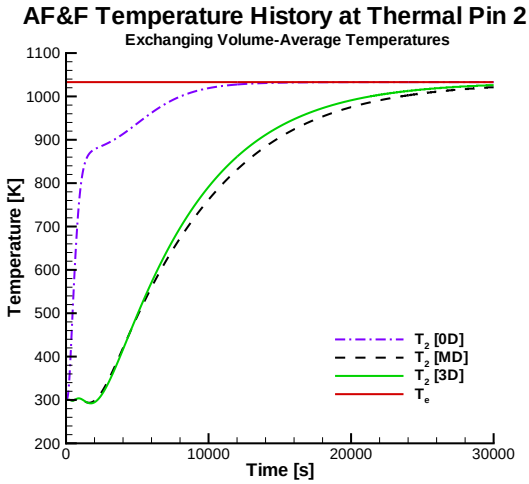

Figure 23. Temperature Histories for Thermal Pin 2 in the AF&F for Heating Case 2 (Exchanging Volume-Average Temperatures in the MD Model).

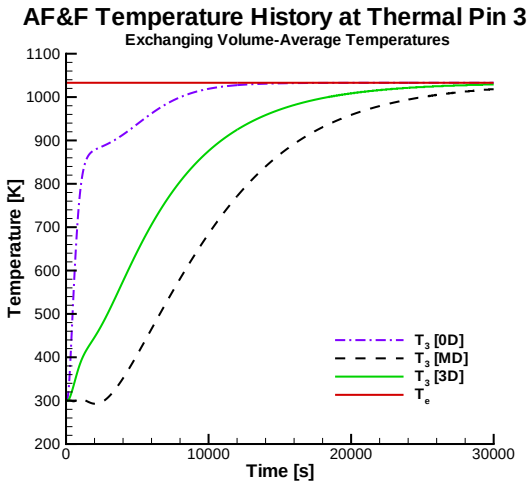

Figure 24. Temperature Histories for Thermal Pin 3 in the AF&F for Heating Case 2 (Exchanging Volume-Average Temperatures in the MD Model).

ature of the AF&F in the 0D model in fact increases more rapidly than the volume-average temperature in the 3D model (Figure 18). These differences are owing to the finite thermal conductivity in the AF&F in the 3D model.

As in the 0D model, the rate of increase in the surface-average temperature of the AF&F in the MD model is decreased by the effect of the package module, which acts as a large thermal sink. This effect is visible in the temperature contours shown in Figure 19, which shows contours on a cross section containing the axis of the AF&F at 3000 s (a time when the difference between the surface-average temperatures of the MD and 3D models is large).

The volume-average temperature for the AF&F in the MD model increases more slowly than the volume-average temperatures for the AF&F in either the 0D or 3D models owing to the finite thermal conductivity in the AF&F in the MD model (which slows the transfer of heat to the interior) and the influence of the package as a large thermal sink (so that there is a net thermal energy transfer from the AF&F to the package) (Figure 18).

We show the maximum and minimum temperatures in the AF&F for the MD and 3D system models in Figures 20 and 21, respectively. The anomalous temperatures at early times (prior to approximately 4000 s) are caused by insufficient mesh resolution (see Section 5.1.1). Except at very early times and at very late times, the maximum AF&F temperatures predicted by the MD and 3D models are significantly different (Figure 20). In

contrast, the minimum temperatures follow similar trends and are somewhat close (Figure 21).

The temperature histories at the three thermal pins in the AF&F (Figure 13) are shown in Figures 22, 23, and 24, respectively. The temperatures predicted by the MD model at Thermal Pin 2 are close to those predicted by the 3D model at that point (Figure 15. However, the temperatures predicted by the MD model at Thermal Pin 1 are not good approximations to the temperatures predicted by the 3D model at Thermal Pin 1, except at very early times and relatively late times (after approximately 10,000 s) (Figure 22). And the temperatures predicted by the MD model at Thermal Pin 3 are not good approximations to the temperatures predicted by the 3D model at Thermal Pin 2.

5.1.3 Conclusions from the Heating Problem

The discussion of model consistency for Heating Case 1 (Section 5.1.1) shows that the determination of model consistency is clearly dependent on the desired metric, which is a function of the intended use of the model. The metric might be the trend of a parameter over some time period(s), or the values of that parameter over some time period(s), or some combination of parameters.

An analysis of volumetric energy conservation given in Appendix 8 suggests that the volume-average temperature should be a good candidate for coupling the three-dimensional component to the zero-dimensional model. However, comparing the results from Heating Case 1 and Heating Case 2, the temperatures predicted for the AF&F when the surface-average temperature is exchanged in the MD model are somewhat better approximations to the temperatures predicted by the 3D model than the temperatures predicted for the AF&F when the volume-average temperature is exchanged in the MD model; compare, for example, Figures 7 and 17, or Figures 8 and 18. This is not surprising because thermal radiation heat transfer is governed by surface temperatures and not temperatures in the interior of a body.

5.2 The Cooling Problem

In the cooling problem, the environment was a constant temperature of 300 K and the system was initially at a temperature of 1033 K.

5.2.1 Cooling Case 1: Exchanging the Surface-Average Temperature

Cooling Case 1 is the case of the cooling problem in which the surface-average temperature of the AF&F was exchanged with the zero-dimensional system model in the MD model.

Figure 25 shows the surface-average temperatures and Figure 26 shows the volume-

average temperatures predicted for the AF&F by the three models for Cooling Case 1. Because the cooling of the AF&F is controlled by radiation to the surrounding bodies, which are all represented by zero-dimensional models in the MD system model, the surface-average and volume-average temperatures for the AF&F in the MD model are close to those for the AF&F in the 0D model (compare Figures 25 and 26). However, owing to the finite thermal conductivity of the AF&F material in the MD model, the volume-average temperature of the AF&F in the MD model is similar to the volume-average temperature of the AF&F in the 3D model (Figure 26).

Temperature contours for the AF&F in the cooling problem for the MD and 3D models at 3000 s are shown in Figure 27. The influence of the package as a relative heat source in the MD model (analogous to its influence as a relative heat sink in the heating problem) is seen in the contours.

Figures 28 and 29 show the maximum and minimum temperatures, respectively, for the AF&Fas a function of time. Although the temperature trends are correct, neither the maximum temperatures nor the minimum temperatures predicted by the MD model are good approximations to the corresponding temperatures predicted by the 3D model. For this problem, the maximum temperature of the AF&F occurs in its interior in both the MD and 3D models, and so the maximum temperatures in both models are similar (refer to the discussion above). However, the minimum temperature of the AF&F occurs on its outer surface, and so the minimum temperature of the AF&F in the MD model is different than the minimum temperature of the AF&F in the 3D model (again, refer to the discussion above).

Figures 30, 31, and 32 show the temperature histories at the thermal pins in the AF&F (see Figure 13). The AF&F in the 0D model cools uniformly and its temperature is uniform. Owing to its finite thermal conductivity, the AF&F in the MD model initially cools like the AF&F in the 3D model, but later behaves thermally more like the AF&F in the 0D model because it is embedded in a system of zero-dimensional models. Although the trends of the temperatures are correct, none of the temperature histories at the thermal pins in the MD model are especially good approximations to the temperature histories predicted by the 3D model at the thermal pins.

5.2.2 Cooling Case 2: Exchanging the Volume-Average Temperature

Cooling Case 2 is the case of the cooling problem in which the volume-average temperature of the AF&F was exchanged with the zero-dimensional system model in the MD model.

Figure 33 shows the surface-average temperatures and Figure 34 shows the volume-average temperatures predicted for the AF&F by the three models for Cooling Case 2, the cooling scenario, in which the volume-average temperature from the three-dimensional AF&F module is sent to the zero-dimensional system model in the MD model. Figure 35

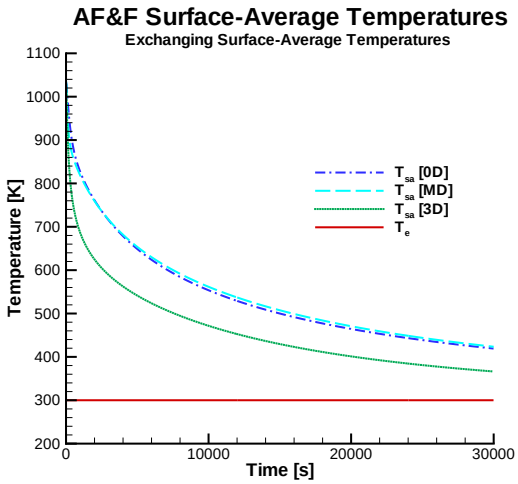

Figure 25. Surface-Average Temperatures for the AF&F in Cooling Case 1 (Exchanging Surface-Average Temperature in the MD Model).

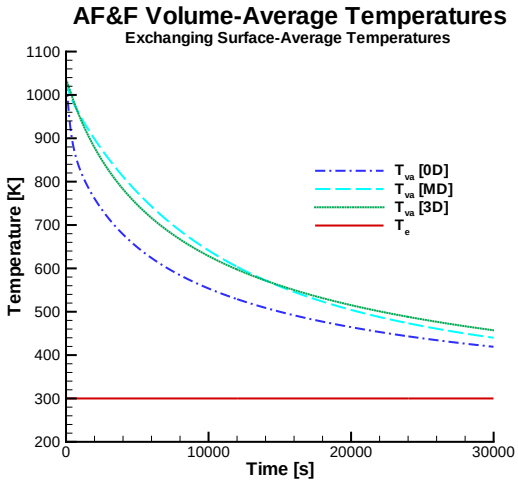

Figure 26. Volume-Average Temperatures for the AF&F in Cooling Case 1 (Exchanging Surface-Average Temperature in the MD Model).

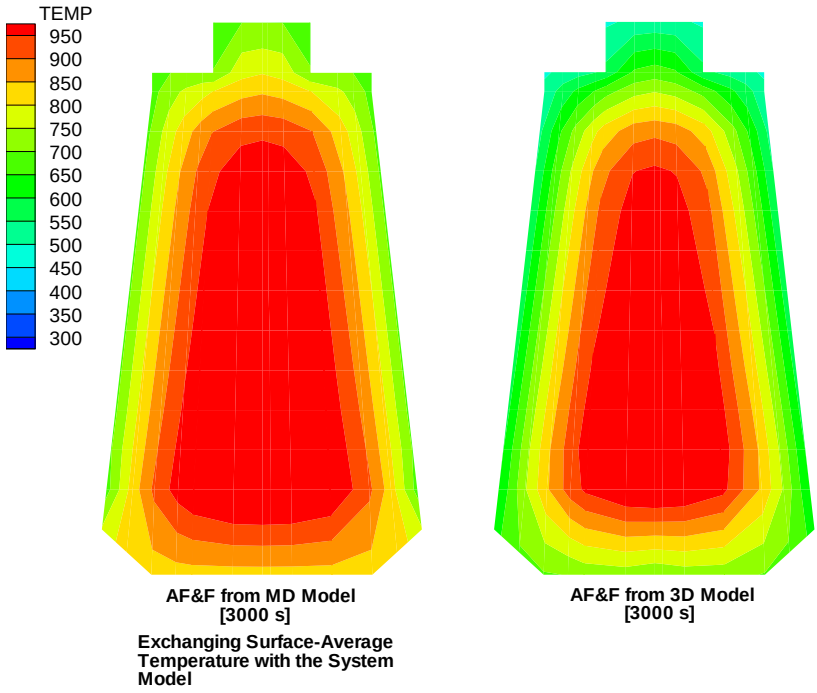

Figure 27. Comparison of Internal Temperatures for the AF&F for the MD and 3D Models for Cooling Case 1 (Exchanging Surface-Average Temperatures in the MD Model) at 3000 s. Left: The MD Model. Right: The 3D Model.

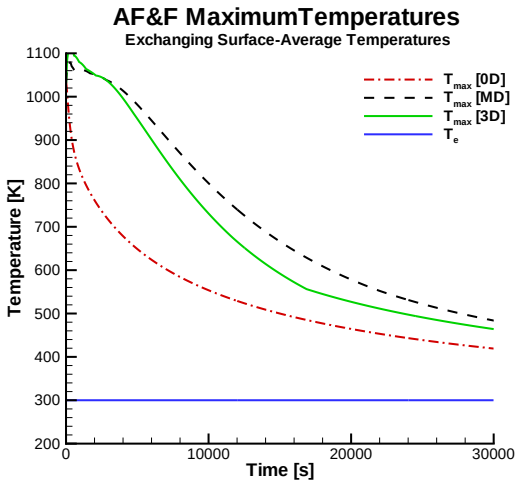

Figure 28. Maximum Temperature in the AF&F for Cooling Case 1 (Exchanging Surface-Average Temperatures in the MD Model).

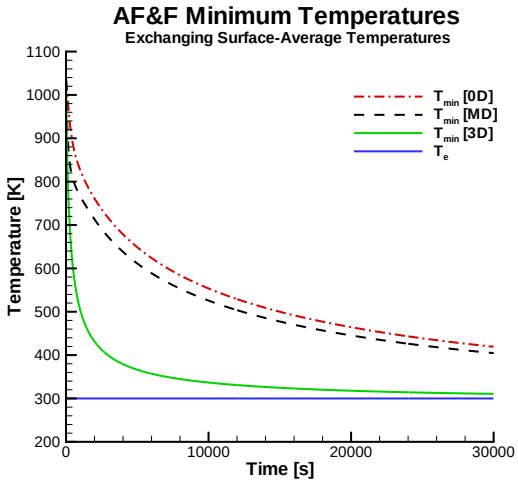

Figure 29. Minimum Temperature in the AF&F for Cooling Case 1 (Exchanging Surface-Average Temperatures in the MD Model).

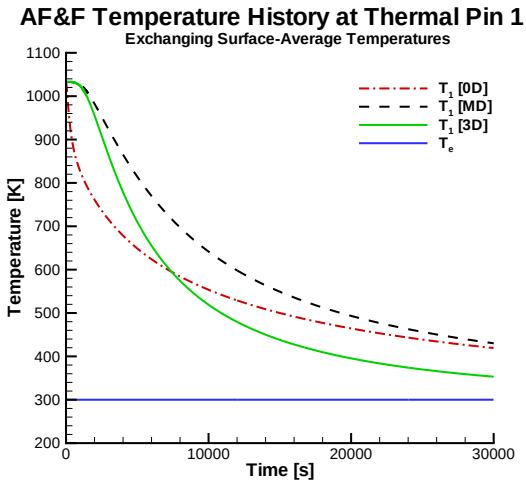

Figure 30. Temperature Histories for Thermal Pin 1 in the AF&F for Cooling Case 1 (Exchanging Surface-Average Temperatures in the MD Model).

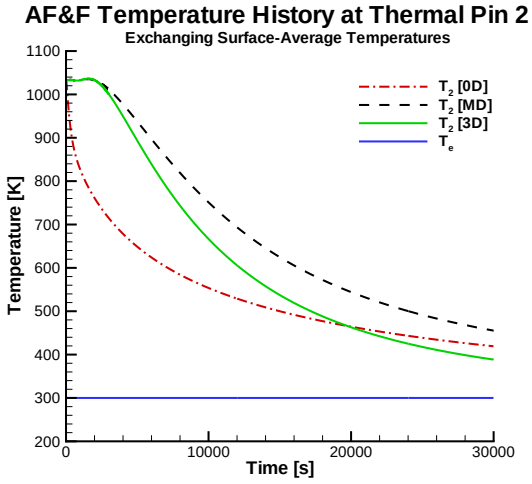

Figure 31. Temperature Histories for Thermal Pin 2 in the AF&F for Cooling Case 1 (Exchanging Surface-Average Temperatures in the MD Model).

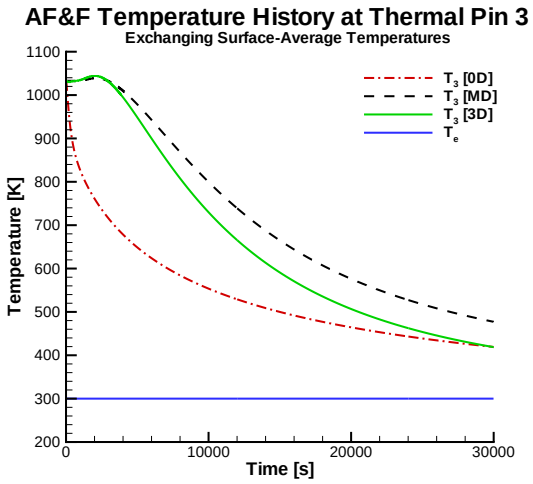

Figure 32. Temperature Histories for Thermal Pin 3 in the AF&F for Cooling Case 1 (Exchanging Surface-Average Temperatures in the MD Model).

shows the internal temperatures for the AF&F at 3000 s. Because the cooling of the AF&F is controlled by radiation to the surrounding bodies, which are all represented by zero-dimensional models in the MD system model, the surface-average and volume-average temperatures for the AF&F in the MD model are close to those for the AF&F in the 0D model (compare Figures 33 and 34).

Temperature contours for the AF&F in Cooling Case 2 for the MD and 3D models at 3000 seconds are shown in Figure 35. The influence of the package as a relative heat source in the MD model is seen in the contours.

We show the maximum and minimum temperatures in the AF&F for Cooling Case 2 in Figures 36 and 37, respectively. Neither the maximum temperatures predicted by the MD model are good approximations to the corresponding temperatures predicted by the 3D model.

The temperature histories at the three thermal pins in the AF&F (Figure 13) are shown in Figures 38, 39, and 40, respectively. Although the trends are correct, none of the temperature histories at the thermal pins in the MD model are especially good approximations to the temperature histories predicted by the 3D model at the corresponding pins.

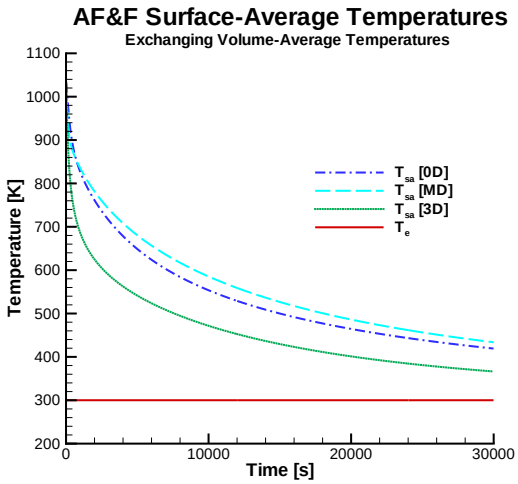

Figure 33. Surface-Average Temperatures for Cooling Case 2 (Cooling Scenario; Exchanging Volume-Average Temperatures).

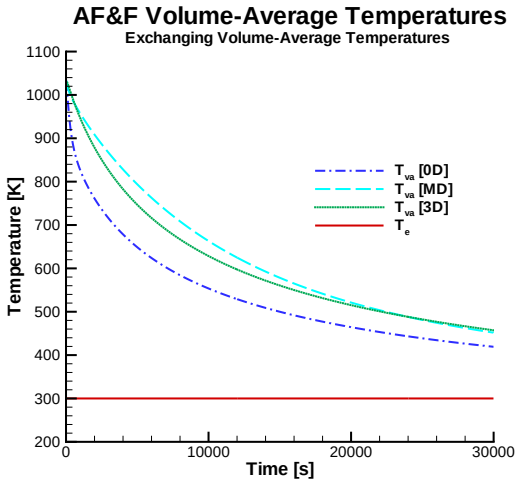

Figure 34. Volume-Average Temperatures for Cooling Case 2 (Cooling Scenario; Exchanging Surface-Average Temperatures).

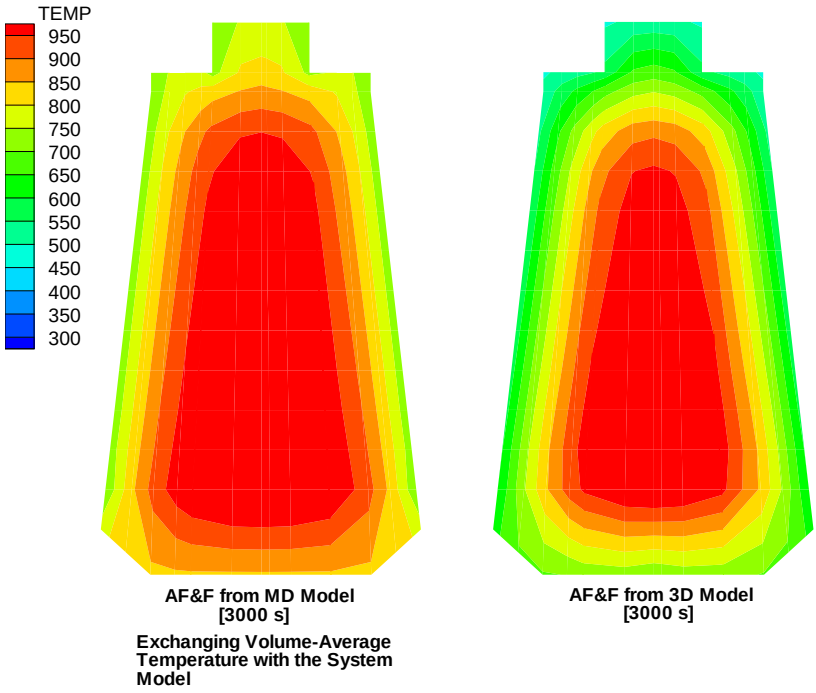

Figure 35. Comparison of Internal Temperatures for the AF&F Predicted by the MD and 3D Models (Exchanging Volume-Average Temperatures in the MD Model) for Cooling Case 2 at 3000 s. Left: The MD Model. Right: The 3D Model.

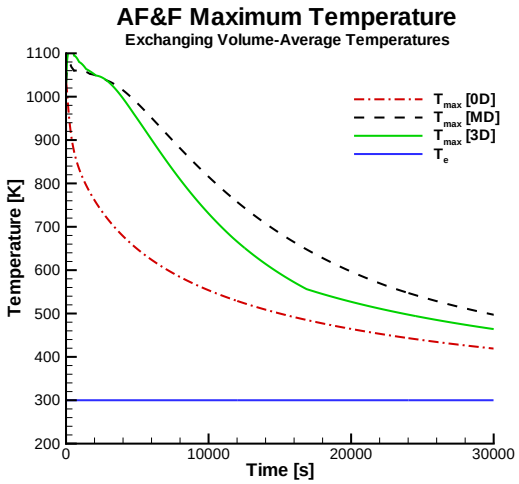

Figure 36. Maximum Temperature in the AF&F for Cooling Case 2 (Exchanging Volume-Average Temperatures in the MD Model).

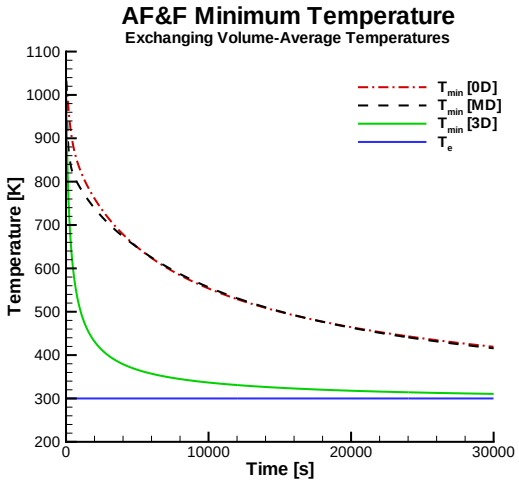

Figure 37. Minimum Temperature in the AF&F for Cooling Case 2 (Exchanging Volume-Average Temperatures in the MD Model).

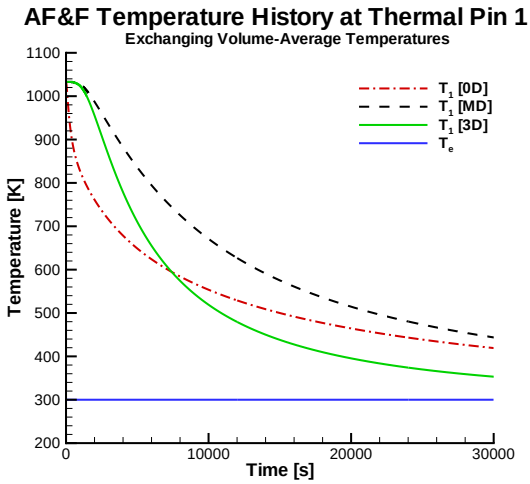

Figure 38. Temperature Histories for Thermal Pin 1 in the AF&F for Cooling Case 2 (Exchanging Volume-Average Temperatures in the MD Model).

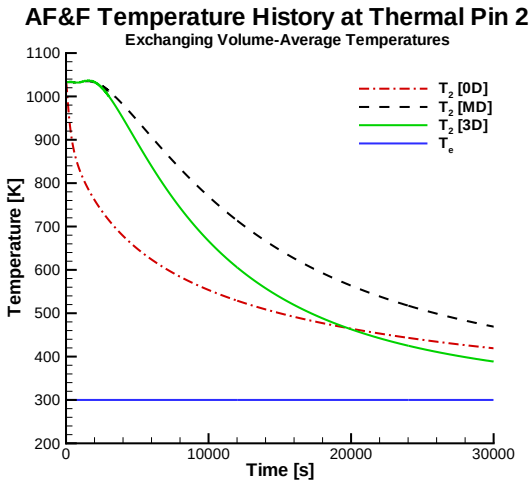

Figure 39. Temperature Histories for Thermal Pin 2 in the AF&F for Cooling Case 2 (Exchanging Volume-Average Temperatures in the MD Model).

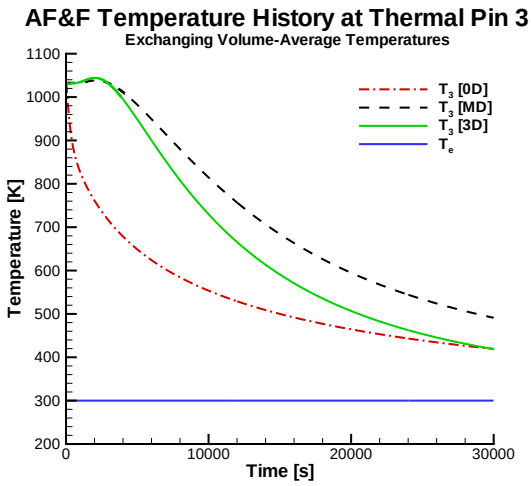

Figure 40. Temperature Histories for Thermal Pin 3 in the AF&F for Cooling Case 2 (Exchanging Volume-Average Temperatures in the MD Model).

5.2.3 Conclusions from the Cooling Problem

As with the heating problem (Section 5.1.3), the temperatures predicted for the AF&F when the surface-average temperature is exchanged in the MD model are somewhat better approximations to the temperatures predicted by the 3D model than the temperatures predicted for the AF&F when the volume-average temperature is exchanged in the MD model; compare, for example, Figures 25 and 33, or Figures 26 and 34. Again, this is not surprising because thermal radiation heat transfer is governed by surface temperatures and not temperatures in the interior of a body.

5.3 The Time-Dependent Boundary Condition Problem

In the time-dependent boundary condition problem, the environment represents a simulated engulfing fire, in which the environment temperature rises rapidly to 1033 K from 300 K, remains at this temperature for a period of time, and then decreases to 300 K.

5.3.1 Fire Case 1: Exchanging the Surface-Average Temperature

Fire Case 1 is the case of the time-dependent boundary condition problem in which the surface-average temperature of the AF&F was exchanged with the zero-dimensional system model in the MD model.

Figure 41 shows the surface-average temperatures and Figure 42 shows the volume-average temperatures predicted for the AF&F by the three system models for the simulated-fire environment, for the case in which the surface-average temperature from the three-dimensional AF&F module is sent to the otherwise zero-dimensional system model in the MD model.

Prior to 10,000 seconds (when the "fire" is "extinguished"), the temperature histories for the 0D, MD, and 3D models are, not surprisingly, similar to those for the heating problem (compare the surface-average temperatures in Figures 7 and 41, and the volume-average temperatures in Figures 8 and 42), because the heating problem and the time-dependent boundary condition problem are essentially the same during this time when the heating period is relatively brief.

The system begins to cool at 10,000 seconds. The cooling is sufficiently rapid that the temperature histories for the 0D, MD, and 3D models are similar to those for the cooling problem (compare the surface-average temperatures in Figures 41 and 25 and the volume-average temperatures in Figures 42 and 26).

5.3.2 Fire Case 2: Exchanging the Volume-Average Temperature

Fire Case 2 is the case of the time-dependent boundary condition problem in which the volume-average temperature of the AF&F was exchanged with the zero-dimensional system model in the MD model.

Figure 49 shows the surface-average temperatures and Figure 50 shows the volume-average temperatures predicted for the AF&F by the three system models for the simulated-fire environment, for the case in which the surface-average temperature from the three-dimensional AF&F module is sent to the otherwise zero-dimensional system model in the MD model.

Prior to 10,000 seconds (when the "fire" is "extinguished"), the temperature histories for the 0D, MD, and 3D models are, not surprisingly, similar to those for the heating problem (compare the surface-average temperatures in Figures 17 and 49, and the volume-average temperatures in Figures 18 and 18), because the heating problem and the time-dependent boundary condition problem are essentially the same during this time when the heating period is relatively brief.

The system begins to cool at 10,000 seconds. The cooling is sufficiently rapid that the temperature histories for the 0D, MD, and 3D models are similar to those for the cooling problem (compare the surface-average temperatures in Figures 49 and 33 and the volume-average temperatures in Figures 50 and 34).

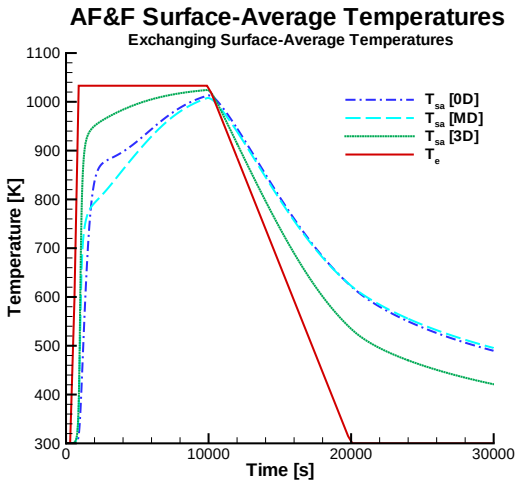

Figure 41. Surface-Average Temperatures for the AF&F for the Time-Dependent Thermal Boundary Condition Problem (Exchanging Surface-Average Temperatures in the MD Model).

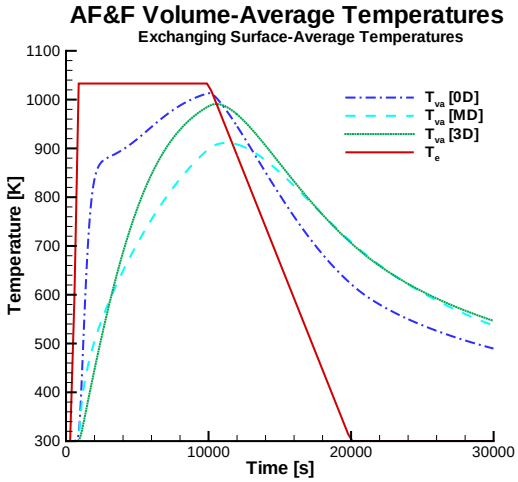

Figure 42. Volume-Average Temperatures for the AF&F for the Time-Dependent Boundary Condition Problem (Exchanging Surface-Average Temperatures in the MD Model).

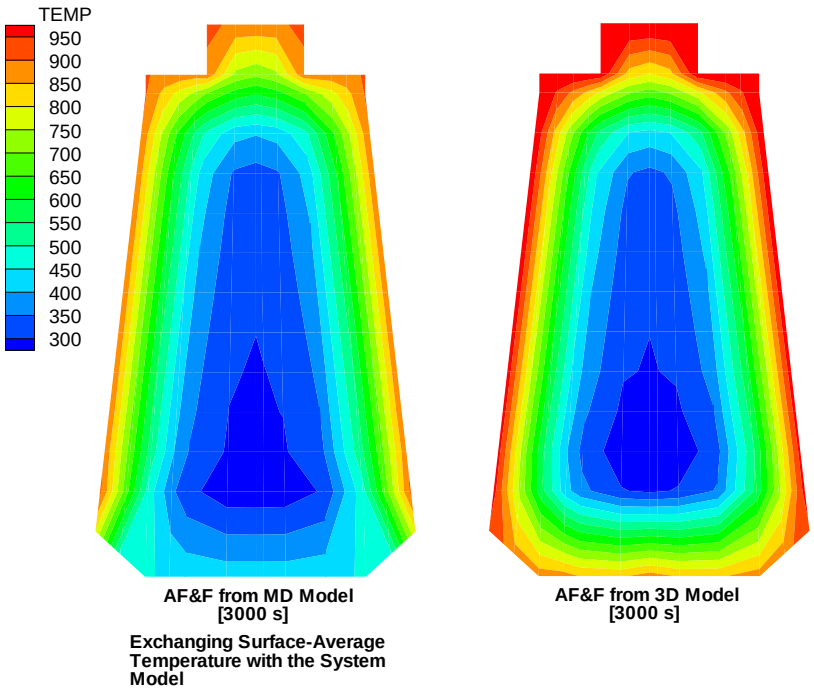

Figure 43. Comparison of Internal Temperatures for the AF&F for the MD and 3D Models for the Time-Dependent Thermal Radiation Boundary Condition Problem (Exchanging Surface-Average Temperatures in the MD Model) at 3000 s. Left: The MD Model. Right: The 3D Model.

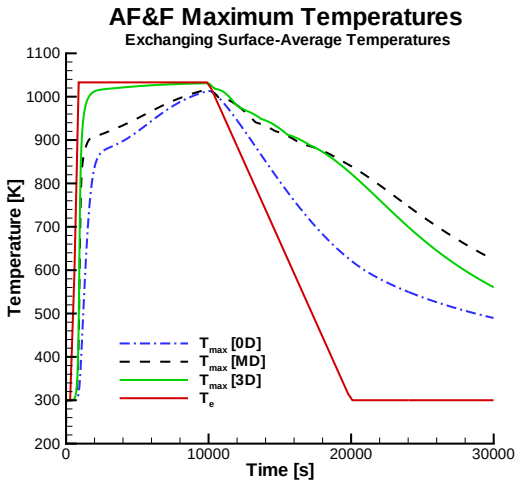

Figure 44. Maximum Temperature in the AF&F for Fire Case 1 (Exchanging Surface-Average Temperatures in the MD Model).

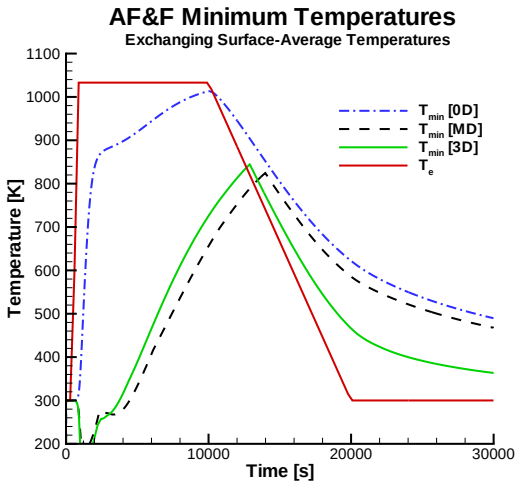

Figure 45. Minimum Temperature in the AF&F for Fire Case 1 (Exchanging Surface-Average Temperatures in the MD Model).

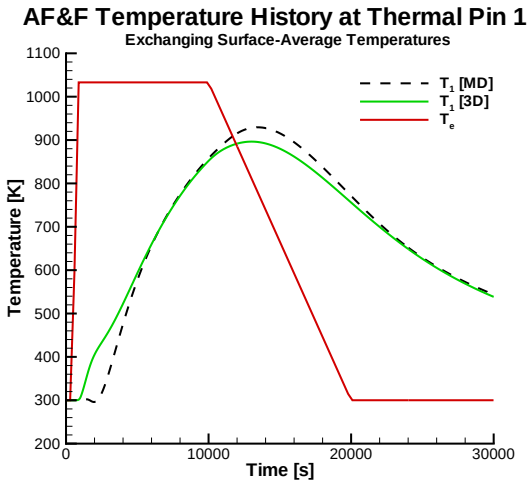

Figure 46. Temperature Histories for Thermal Pin 1 in the AF&F for Fire Case 1 (Exchanging Surface-Average Temperatures in the MD Model).

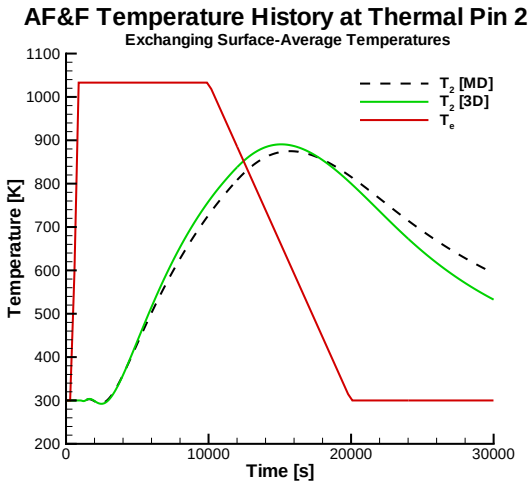

Figure 47. Temperature Histories for Thermal Pin 2 in the AF&F for Fire Case 1 (Exchanging Surface-Average Temperatures in the MD Model).

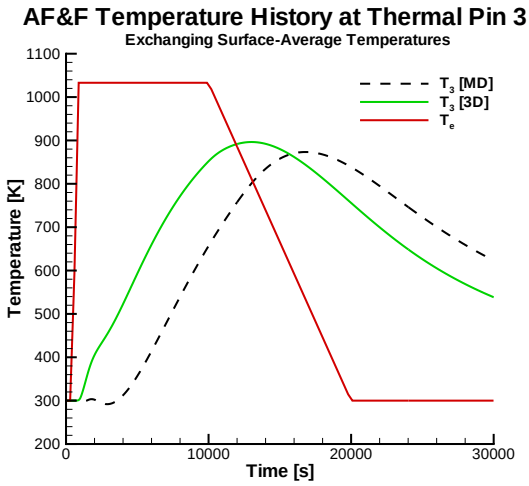

Figure 48. Temperature Histories for Thermal Pin 3 in the AF&F for Fire Case 1 (Surface Volume-Average Temperatures in the MD Model).

5.3.3 Conclusions from the Time-Dependent Boundary Condition Problem

As with the heating and cooling problems (Sections 5.1.3 and 5.2.3), the temperatures predicted for the AF&F when the surface-average temperature is exchanged in the MD model are somewhat better approximations to the temperatures predicted by the 3D model than the temperatures predicted for the AF&F when the volume-average temperature is exchanged in the MD model; compare, for example, Figures 41 and 49, or Figures 42 and 50. Again, this is not surprising because thermal radiation heat transfer is governed by surface temperatures and not temperatures in the interior of a body.

5.4 Simulation Timing Results

In Table 2 we give simulation timing results for the three cases summarized above. We ran all the calculations on a single processor of a Dell workstation with a 1.3 GHz Intel Pentium 4 processor, and each simulation produced the output files considered typical for the simulation. For example, the mixed-fidelity and three-dimensional system models each produced an output file containing mesh temperatures.

Referring to Table 2, the MD model ran over 25 times faster than the 3D model on the Dell workstation (in under three minutes compared to over an hour) and provides internal temperatures for the higher fidelity module. These results indicate that optimization studies with mixed-fidelity models are feasible when they may not be feasible with three-dimensional system models.

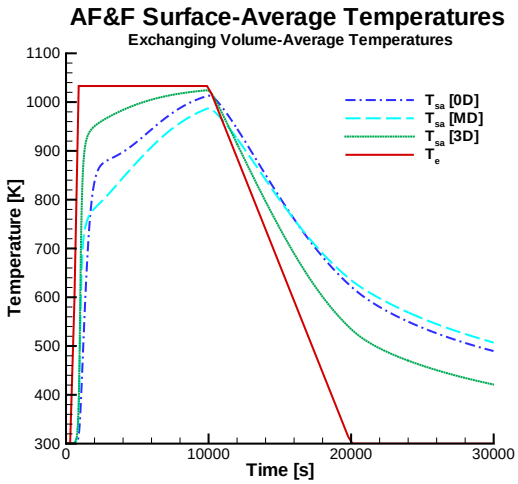

Figure 49. Surface-Average Temperatures for the AF&F for Fire Case 2 (Exchanging Volume-Average Temperatures in the MD Model).

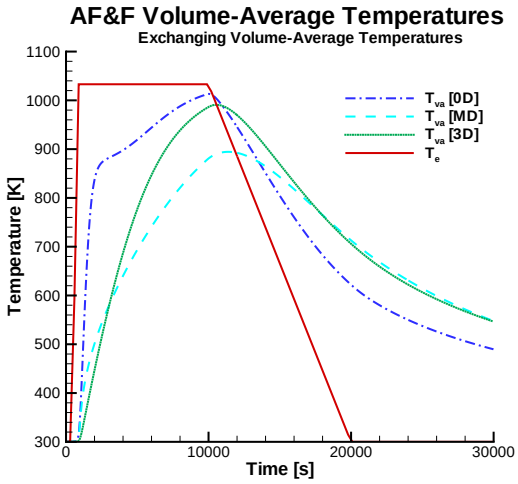

Figure 50. Volume-Average Temperatures for the AF&F for Fire Case 2 (Exchanging Volume-Average Temperatures in the MD Model).

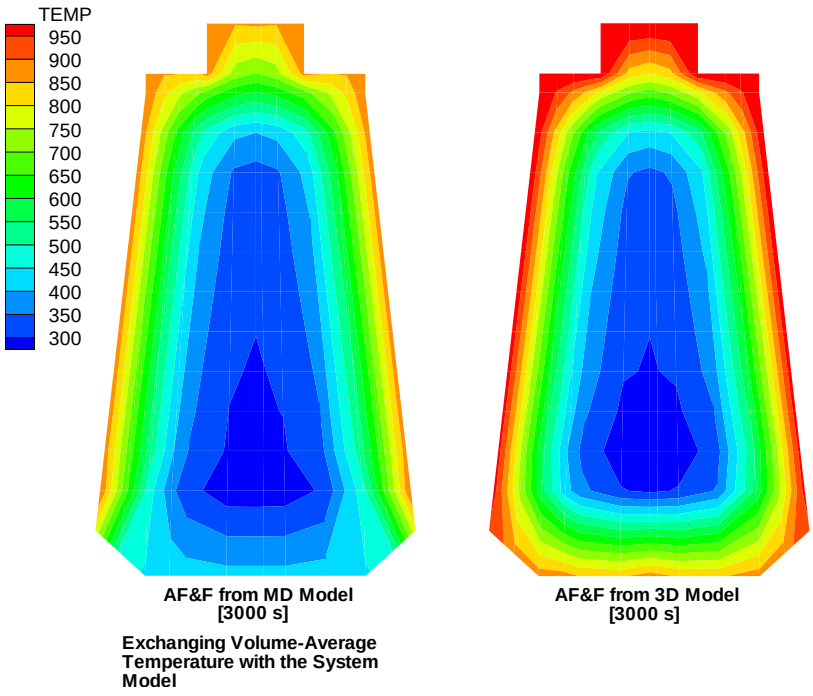

Figure 51. Comparison of Internal Temperatures for the AF&F for the MD and 3D Models for Fire Case 2 (Exchanging Volume-Average Temperatures in the MD Model) at 3000 s. Left: The MD Model. Right: The 3D Model.

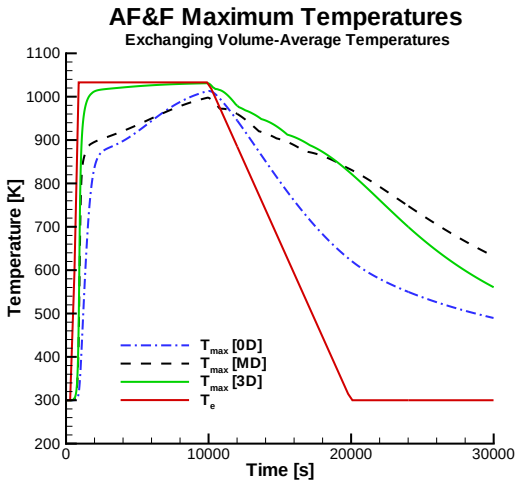

Figure 52. Maximum Temperature in the AF&F for Fire Case 2 (Exchanging Surface-Average Temperatures in the MD Model).

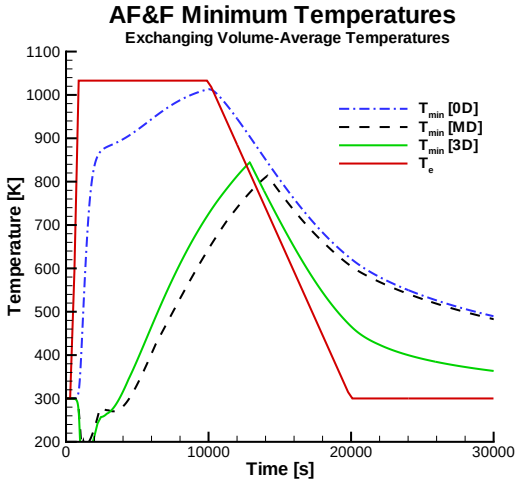

Figure 53. Minimum Temperature in the AF&F for Fire Case 2 (Exchanging Surface-Average Temperatures in the MD Model).

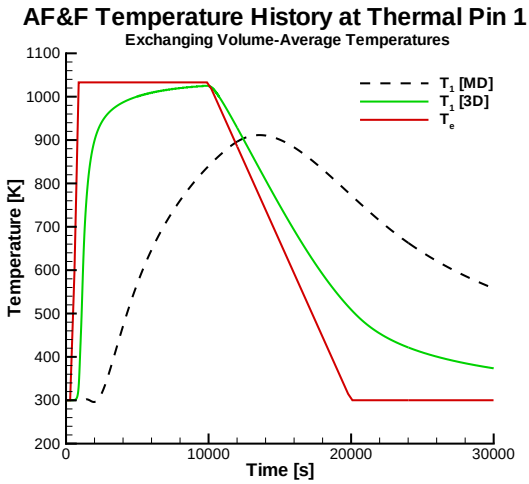

Figure 54. Temperature Histories for Thermal Pin 1 in the AF&F for Fire Case 2 (Exchanging Surface-Average Temperatures in the MD Model).

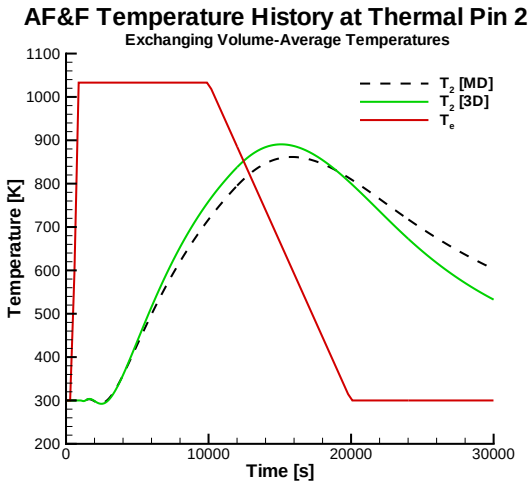

Figure 55. Temperature Histories for Thermal Pin 2 in the AF&F for Fire Case 2 (Exchanging Volume-Average Temperatures in the MD Model).

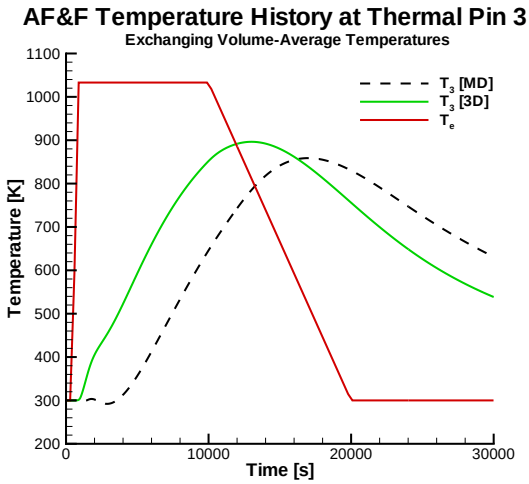

Figure 56. Temperature Histories for Thermal Pin 3 in the AF&F for Fire Case 2 (Exchanging Volume-Average Temperatures in the MD Model).

Table 2. CPU Times for the Test Cases.

	System Model				
	0D Only	Mixed-Fidelity			3D Only[a]
		3D Model	0D Model	Total	
Case	[s]	[s]	[s]	[s]	[s]
Heating	0.22	170.10	0.58	170.68	3931.
Cooling	0.31	171.45	0.85	172.30	3904.
“Fire”	0.24	168.55	0.97	169.52	3904.

[a] Does not include time to calculate the view factors (35.1 hrs).

6 Implementation of the Multifidelity Algorithm in the *Entero* Software

The mixed-fidelity algorithm for thermal radiation was implemented in the *Entero* software as part of a prototype for multifidelity, multiphysics environments for thermal analysis of systems containing electrical circuits and exposed to fires [5, 7].

With the software, the user starts from an initial system (provided with the software or previously saved by the user) and can add or delete components (subject to composition rules enforced by the software), and add or delete connections, or "ports," between components. The user is guided through this process by a series of software wizards. Components of the system are represented by zero-dimensional thermal models; the user can replace one of the components with a three-dimensional, finite-element model, which is connected to the zero-dimensional system model by a mixed-fidelity port.

The dimensions and relative locations of the zero-dimensional models (which are represented as conical frustums) can be adjusted by the user with a geometry editor. View factors are automatically calculated for the zero-dimensional models. The user can modify the mass and thermal properties of individual components (*e.g.*, density and specific heat capacity).

The user can embed electrical circuits in each of the components, and for the three-dimensional model can specify the circuit location; the circuit is connected to a component using a multiphysics port.

Following system set up, the user can analyze the system and monitor the temperatures in the components and the electrical activity in the circuit as the simulation progresses. An example of the user interface is shown in Figure 57.

7 Summary and Conclusions

Modeling and simulation of complex systems at various levels of fidelity is increasingly important at Sandia National Laboratories in fulfilling its national security mission. In this report we described the development of a mixed-fidelity algorithm for thermal radiation heat transfer. Using the algorithm, a three-dimensional finite-element model for a component can be embedded in a zero-dimensional system model.

Mixed-fidelity models have several advantages. They enable a component design to be evaluated in the context of a full system, and allow more realistic boundary conditions for the model of the component. They enable more rapid system-level analysis and optimization, because changes to the higher fidelity model can be incorporated directly into the system model without constructing an equivalent lower fidelity model. They enable

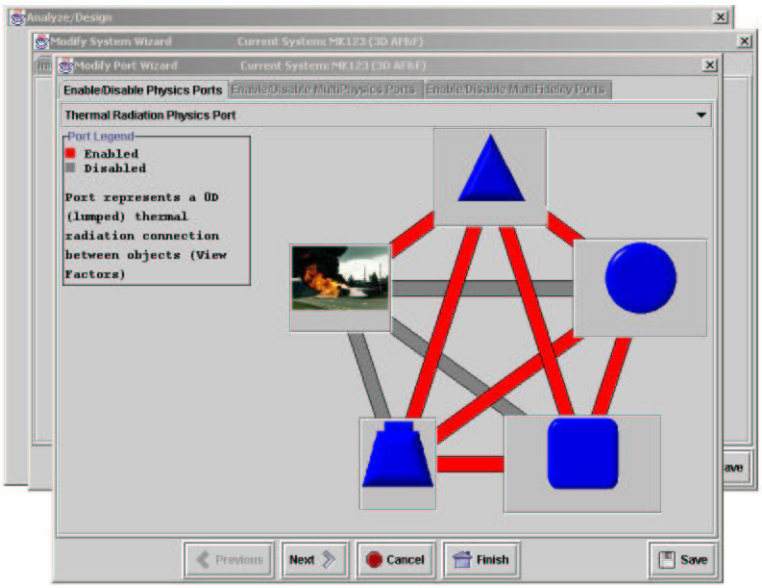

Figure 57. The *Entero* User Interface for Coupled Thermal-Electrical Modeling.

the uncertainty in knowledge of a component to be reflected in the fidelity of the model used for the component, independent of the fidelities of models used for other components. And the resolution and fidelity of the simulation can be tailored to the requirements of the analysis, using lower fidelity models for exploratory studies and hence making better use of computing and personnel resources [8, 9].

However, as discussed in Section 3, mixed-fidelity algorithms also have some drawbacks. These include challenges in integrating models with differing spatial dimensionalities and resolutions, integrating physics and models with differing time scales, determining the consistency of multifidelity models, and verifying and validating multifidelity models.

In particular we highlighted the difficulty in determining the consistency of mixed-fidelity models. The difficulty arises from the multiplicity of possible measures of consistency.

The version of the mixed-fidelity algorithm in which the surface-average temperature of the three-dimensional model was exchanged with the zero-dimensional system model provided somewhat better predictions of the temperature metrics than did the version in which the volume-average temperature was exchanged with the zero-dimensional system model.

A mixed-fidelity system model can potentially execute much faster than a full three-

dimensional finite-element model for thermal radiation problems and provides internal temperatures for the higher fidelity module. However, there is some loss in accuracy with the mixed-fidelity system model. These results indicate that optimization studies with mixed-fidelity models are feasible when they may not be feasible with three-dimensional system models, if the concomitant loss in accuracy is within acceptable bounds.

The mixed-fidelity algorithm for thermal radiation was implemented in the *Entero* software as part of a prototype environment for multifidelity, multiphysics environment for thermal analysis of systems containing electrical systems and exposed to fires [5, 7]. The software allows the user considerable flexibility in creating and modifying system models, and in monitoring the temperatures in the components and the electrical activity in the embedded circuit as a simulation progresses.

The multifidelity algorithm for thermal radiation could be extended to conductive heat transfer using the concept of a one-dimensional "thermal wire" to connect two modules in a system. In a thermal wire, conduction occurs only along its length, and its cross-sectional area as a function of length is specified. This construct can be connected to a three-dimensional finite-element mesh using either the surface-average temperature or an average surface temperature for the area of contact. The latter connection could be implemented using a flux boundary condition on an element side set, and might provide increased accuracy in the temperature predictions.

In summary, the mixed-fidelity model ran sufficiently fast with sufficient accuracy to enable design optimization studies for coupled thermal/electrical modeling. Further studies to verify this conclusion are warranted.

Table 3. Geometric Parameters for the Case.

Case	
Frustum of a cone	
Radius $r = 0.2$ m	
Height $h = 1.0$ m	
Thickness $a = 0.01$ m	
Half angle, $\theta = \arctan(r/h)$	$\theta = 0.1973^{\mathrm{R}}$
Enclosed volume, $V_i = \pi r^2 h/3$	$V_i = 0.2094$ m^3
Interior Area, $A_i = \pi r(r + h/\cos\theta)$	$A_i = 0.7664$ m^2
Exterior Area, $A_o = \pi r(r + h/\cos\theta)(1 + \frac{a\gamma}{h})^2$ $= A_i(1 + \frac{a\gamma}{h})^2$	$A_o = 0.7673$ m^2
Shell Volume, $V_s = \pi r^2 h\gamma(1 + \gamma + \gamma^2/3)$	$V_s = 8.141\times10^{-3}$ m^3
$\gamma = a(1 + \sin^{-1}\theta)/h$	$\gamma = 6.099\times10^{-2}$

Appendix 1: Geometric Dimensions and Material Properties for the Test System

The geometry for the test system is shown in Figure 2. It consists of four component modules: a safety device, an AF&F, and a package enclosed within a case module. The case is a conical shell. The other modules are frustums of cones. Dimensions for each module are given in Tables 3–6. In the test system, all the modules are coaxial, with positions measured from the interior apex of the case given in Table 7.

The materials and properties for each of the modules are listed in Table 8. Densities, thermal conductivities, and specific heat capacities are taken from Reference [38, Table A.3], and emissivities are taken from Reference [39, Appendix D], unless otherwise noted. Note that the lumped-parameter models assume that all surfaces are black and hence all the emissivities are 1.0.

Table 4. Geometric Parameters for the Package.

Package	
Frustum of a cone	
Upper radius $r_1 = 0.1062$ m	
Lower radius $r_2 = 0.1880$ m	
Height $h = 0.4089$ m	
Half angle, $\theta = \arctan((r_2 - r_1)/h)$	$\theta = 0.1973^{\mathrm{R}}$
Area, $A = \pi(h(r_1 + r_2)/\cos\theta + r_1^2 + r_2^2)$	$A = 5.319\times10^{-1}$ m^2
Volume, $V = \pi h({r_1}^2 + r_1 r_2 + {r_2}^2)/3$	$V = 2.851\times10^{-2}$ m^3

Table 5. Geometric Parameters for the AF&F.

AF&F	
Frustum of a cone	
Upper radius $r_1 = 0.052$ m	
Lower radius $r_2 = 0.082$ m	
Height $h = 0.27113$ m	
Half angle, $\theta = \arctan((r_2 - r_1)/h)$	$\theta = 0.1086^{\mathrm{R}}$
Area, $A = \pi(h(r_1 + r_2)/\cos\theta + r_1^2 + r_2^2)$	$A = 1.444\times10^{-1}$ m^2
Volume, $V = \pi h({r_1}^2 + r_1 r_2 + {r_2}^2)/3$	$V = 3.875\times10^{-3}$ m^3

Table 6. Geometric Parameters for the Safety Device.

Safety Device	
Frustum of a cone	
Upper radius $r_1 = 0.020$ m	
Lower radius $r_2 = 0.048$ m	
Height $h = 0.140$ m	
Half angle, $\theta = \arctan((r_2 - r_1)/h)$	$\theta = 0.1973^{\mathrm{R}}$
Area, $A = \pi(h(r_1 + r_2)/\cos\theta + r_1^2 + r_2^2)$	$A = 3.899\times10^{-2}$ m^2
Volume, $V = \pi h({r_1}^2 + r_1 r_2 + {r_2}^2)/3$	$V = 5.372\times10^{-4}$ m^3

Table 7. Module Positions in the test system.

Module	Position [m]
Safety Device	0.150
AF&F	0.300
Package	0.581113

Note: All positions are measured from the interior apex of the case to the upper surface of the module. The “upper” surface of a module is the one with the upper radius. See Tables 3–6.

Table 8. Materials and Properties[a] for the Fictitious Test System.

Module	Material	Density [kg/m^3]	Thermal Conductivity [W/m-K]	Specific Heat Capacity [J/kg-K]	Emissivity
Case	Graphite fiber epoxy[b]	2210.0	5.70[c]	935.0	0.9[d]
Package	Stainless Steel (304)[e]	7900.0	14.9	700.0	0.16[f]
AF&F	Oak[g]	545.0	0.17	2385.0	0.75[h]
Safety Device	Sandstone[i]	2150.0	2.90	745.0	0.83[j]

[a] All properties at 300 K unless otherwise noted.
[b] From Reference [38, Table A.2].
[c] Perpendicular to fibers.
[d] Estimated from values for dielectrics in Reference [39, Appendix D].
[e] From Reference [38, Table A.1].
[f] Polished 301 stainless steel at 297 K, Reference [39, Appendix D].
[g] From Reference [38, Table A.3].
[h] Planed oak, Reference [39, Appendix D].
[i] From Reference [38, Table A.3].
[j] Sandstone at 310 K, Reference [39, Appendix D].

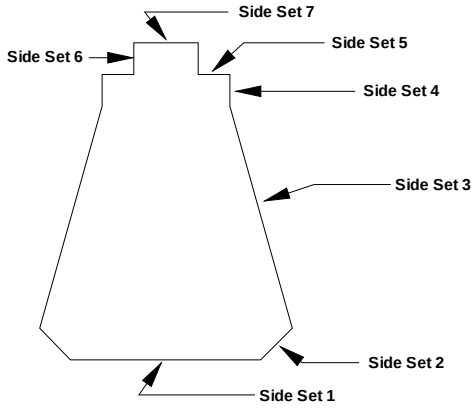

Figure 58. Side Sets in the Mesh for the Three-Dimensional AF&F Module.

Appendix 2: Implementation of the Multifidelity Algorithm

The zero-dimensional system model is called the *integrator* in the *Entero* architecture. The *Entero* integrator for thermal radiation problems is described in [6]. The current version of the integrator allows one interior module in a system to be replaced by a finite-element model. Reference temperatures for the finite-element model are mapped to the external boundaries of the finite-element mesh.

We developed a special version of the Coyote heat transfer code [37, 40] for the mixed-fidelity modeling. We modified the user-defined subroutine USRTRR to provide the reference temperatures via Parallel Virtual Machine (PVM) messages [41] from the zero-dimensional models. We wrote subroutines to compute the surface-average temperature and volume-average temperature of a mesh block.

Currently all the lump temperatures are sent to Coyote through USRTRR and the unnecessary one is discarded in mapping the reference temperatures to the surface node sets. The mapping of side sets of the AF&F mesh to the zero-dimensional models is currently hard-coded in USRTRR. The locations of the side sets are shown in Figure 58. The mappings of the side sets to modules is given in Table 9.

A subroutine SRFAVGT was written to compute the surface-average temperature and inserted just before the calls to USRWRT in the SOLVE subroutine. Surface-average temperatures were calculated as described in Appendix 7.

Table 9. Mappings of Modules to Side Sets in the Test System.

Module Name	Module No.	Maps to Side Sets
Case	1	3, 4
Package	2	1, 2
AF&F	3	—
Safety Device	4	5, 6, 7

A subroutine `VOLAVGT` was written to compute the volume-average temperature and inserted just before the calls to `USRWRT` in the `SOLVE` subroutine. Volume-average temperatures were calculated as described in Appendix 8.

The subroutine `USRWRT` was modified to provide the data for special points. Locations of the points are communicated once (because usually the mesh is static), and temperature values at the points are sent to the integrator every time step.

To activate the special features for mixed-fidelity modeling, certain entries must appear in the Coyote input files. These entries tell Coyote to use the user-specified reference temperature for the exterior surfaces of the mesh and to write user-specified quantities (*i.e.*, the special points) using `USRWRT`. In other words, these entries signal Coyote to expect a link to the lumped-parameter models.

Coyote's user constants are used to select various options. `ICONST(1)` is used to specify where a full three-dimensional model (`ICONST(1) = 1`) or a mixed-fidelity model (`ICONST(1) > 1`) is used.

`ICONST(2)` is used to specify which temperature is passed to the mixed-fidelity model. No temperature is passed if `ICONST(2) = 0`. The volume-average temperature is passed if `ICONST(2) = 1`. The surface-average volume is passed if `ICONST(2) = 2`. Note that `ICONST(2) = 0` should only be used with a full three-dimensional model (`ICONST(1) = 1`).

`ICONST(3)` is used to specify the number of modules, and is only used when a mixed-fidelity model is specified. In this case, `ICONST(3)` is set to 1.

The `SRFAVGT` subroutine computes the surface-average temperature for the mesh defining the module. It processes all the external element faces for each element block.

In addition, the `Write User File` command must appear in the Coyote post processing input block so that the `USRWRT` and `TAVERAGE` subroutines are called by Coyote.

The `Radiation` boundary condition command is used to tell Coyote to use the user-specified reference temperature. Currently, the user must define in the mesh file a collection of disjoint element sets whose union includes all the surface elements of the mesh. Then the `Heat Source` boundary is used to tell Coyote to use the reference temperatures provided by the lumped-parameters models. The command has the form

```
BCType=Radiation,SIDE=sideset_number,COEFficient=1,TREFerence=USER
```

where `sideset_number` is the number of a surface element set. There must be one boundary condition line for each element set that defines part of the surface.

Special points can be used to extract temperatures from the mesh. They can be used to pass temperatures to a circuit simulation code. To specify special points, use the special point command in the problem definition input block:

```
Special Output=N, x1,y1,z1 [,x2,y2,z2,...,xN,yN,ZN]
```

Note that the integrator and Coyote must use the same number of time steps. Currently this is implemented by having the integrator generate the input file named `basename.i` from a template file named `basename.i.m4` (where `basename` is the base name of the simulation and is distinct from the Coyote simulation base name) using `m4` after it reads the input file and determines the number of time steps. Therefore, changes to the input file must be made in the template file if they are to take effect when Coyote is executed.

Appendix 3: Coupling Electronics Modeling to Modules in the System

The *Entero* integrator provides the option of embedding an electronic circuit in any of the modules defining the system. The user specifies the circuit using a standard Spice netlist file [42], and specifies the location of the circuit in the module through the input file using a construct called a *thermal pin*, which is a point in the module.

A zero-dimensional model can have only one thermal pin and its temperature value is the temperature of the model. This pin is automatically defined when the electronics model is linked to the thermal model.

For a higher-dimensional Coyote model, the default number of pins is one, with the temperature value of the surface node-averaged temperature. The user can specify thermal pins at specific locations in the finite element mesh by using the Coyote special points, which are user-defined locations in the mesh. In the case where a thermal pin is specified using a special point, the temperature of the thermal pin is the temperature computed for the special point.

Circuit modeling is performed with the Xyce™ parallel circuit simulator [43].

To link the electronics model to the thermal model, the following lines must be present in the input file for the integrator:

```
electronics = true
circuit_file = filename
```

where `filename` is the name of the file that contains a Spice netlist. This file is processed by the `Unix m4` utility to substitute the value of temperature pin J for the string `PINTEMPJ` and to substitute the value of the variable to be monitored at pin J for the string `PINVARJ` and create a temporary Spice input file in the directory `/tmp` called `EnteroElectronics.inp`. The output from Spice is placed in `/tmp` in `EnteroElectronics.out` and error output is captured in the file `EnteroElectronics.err`. Plotting output is saved in the file `e_filename`, where `filename` is the standard plotting output file specified on the command line (see Appendix 2).

Appendix 4: Calculation of View Factors for the Mixed-Fidelity System Model

Approximate values for view factors were calculated as described in Section 7. Michael F. Young calculated more exact values for the view factors; these are presented in Section A4.2.

A4.1 Calculation of Approximate View Factors

The view factors were calculated assuming that each module sees only the modules immediately adjacent to it. For the configuration shown in Figure 2, the module connectivities are given in Table 10. The configuration factors, or view factors, were then calculated using the areas of the modules, based on the assumed geometric shape.

More formally, the view factors were calculated using the following assumptions:

1. Each body receives thermal radiation only from adjacent bodies. Thus $F_{2-4} = F_{4-2} = 0$.
2. All the thermal energy leaving the surface of the AF&F adjacent to the package reaches only the package.
3. All the thermal energy leaving the surface of the safety device adjacent to the AF&F reaches only the AF&F.
4. The AF&F, package, and safety device modules are convex. Thus $F_{2-2} = 0$, $F_{3-3} = 0$, and $F_{4-4} = 0$.

For the modules with the shape of a frustum of a cone, the "top" surface is the one closest to the case apex; its area is denoted A_{ti}, where i is the module number.

The "bottom" surface is the one closest to the case base; its area is denoted A_{bi}. The remaining surface is the "side" surface; its area is denoted A_{si}. The total surface area is denoted A_i.

For historical reasons, the case is denoted module 1, the package is denoted module 2, the AF&F is denoted module 3, and the safety device is denoted module number 4. The view factor from module i to module j is then denoted F_{i-j}.

A6.1.1 The Safety Device

All the thermal radiation leaving the surface with the larger radius is assumed to reach only the surface of the AF&F with the smaller radius (Assumption 3). Surface areas for the

Table 10. Module Connectivities in the test system.

	Case	Package	AF&F	Safety Device
Case	✓	✓	✓	✓
Package	✓		✓	
AF&F	✓	✓		✓
Safety Device	✓		✓	

safety device are given in Table 11.

The fraction of thermal energy leaving the safety device and reaching the AF&F can therefore be determined from

$$\sigma T_4^4 A_{b4} = \sigma T_4^4 A_4 F_{4-3}$$

or

$$F_{4-3} = A_{b4}/A_4 = 1.856\times10^{-1}$$

All the thermal radiation leaving the remaining surfaces of the safety device is assumed to reach only the interior surface of the case (Assumption 1). From conservation of energy,

$$F_{4-1} + F_{4-2} + F_{4-3} + F_{4-4} = 1$$

$F_{4-2} = 0$ (Assumption 1) and $F_{4-4} = 0$ (Assumption 4). Therefore

$$\begin{aligned} F_{4-1} &= 1 - F_{4-3} \\ &= 1 - 1.856\times10^{-1} \\ &= 8.144\times10^{-1} \end{aligned}$$

A4.1.2 The AF&F

All the radiation leaving the surface of the AF&F with the larger radius is assumed to reach only the surface of the package with the smaller radius (Assumption 2). Surface areas for the AF&F are given in Table 12.

Thus the fraction of thermal energy leaving the AF&F and reaching the package can be determined from

$$\sigma T_3^4 A_{b3} = \sigma T_3^4 A_3 F_{3-2}$$

Table 11. Areas for the Safety Device.

Surface	Area [m^2]
Upper Surface, A_{t4}	1.257×10^{-3}
Lower Surface, A_{b4}	7.238×10^{-3}
Side Surface, A_{s4}	3.050×10^{-2}
Total Surface, A_4	3.899×10^{-2}

Note: The upper surface is the one closest to the apex of the case. The lower surface is the one closest to the base of the case.

or

$$F_{3-2} = A_{b3}/A_3 = 1.463\times10^{-1}$$

By reciprocity [39],

$$A_3F_{3-4} = A_4F_{4-3}$$

or

$$\begin{aligned} F_{3-4} &= F_{4-3}A_4/A_3 \\ &= \left(1.856\times10^{-1}\right)\left(3.899\times10^{-2}\ \mathrm{m}^2/1.444\times10^{-1}\ \mathrm{m}^2\right) \\ &= 5.011\times10^{-2} \end{aligned}$$

All the radiation leaving the side surface of the AF&F is assumed to reach only the interior surface of the case (Assumption 1). From conservation of energy,

$$F_{3-1} + F_{3-2} + F_{3-3} + F_{3-4} = 1$$

$F_{3-3} = 0$ (Assumption 4). Therefore

$$\begin{aligned} F_{3-1} &= 1 - F_{3-2} - F_{3-4} \\ &= 1 - 1.463\times10^{-1} - 5.011\times10^{-2} \\ &= 8.036\times10^{-1} \end{aligned}$$

A4.1.3 The Package

View factors for the package can be calculated from the assumptions and the view factors calculated for the AF&F (Section 7). Surface areas for the package are given in Table 13.

Table 12. Areas for the AF&F.

Surface	Area [m^2]
Upper Surface, A_{t3}	8.495×10^{-3}
Lower Surface, A_{b3}	2.112×10^{-2}
Side Surface, A_{s3}	1.148×10^{-1}
Total Surface, A_3	1.444×10^{-1}

Note: The upper surface is the one closest to the apex of the case. The lower surface is the one closest to the base of the case.

By reciprocity [39],

$$A_2F_{2-3} = A_3F_{3-2}$$

or

$$\begin{aligned} F_{2-3} &= F_{3-2}A_3/A_2 \\ &= \left(1.463\times10^{-1}\right)\left(1.444\times10^{-1}\ \mathrm{m}^2/5.319\times10^{-1}\ \mathrm{m}^2\right) \\ &= 3.972\times10^{-2} \end{aligned} \tag{1}$$

All thermal radiation leaving the remaining surfaces of the package is assumed to reach only the interior surface of the case (Assumption 1).

From conservation of energy,

$$F_{2-1} + F_{2-2} + F_{2-3} + F_{2-4} = 1$$

$F_{2-2} = 0$ (Assumption 4) and $F_{2-4} = 0$ (Assumption 1). Therefore

$$\begin{aligned} F_{2-1} &= 1 - F_{2-3} \\ &= 1 - 3.972\times10^{-2} \\ &= 9.603\times10^{-1} \end{aligned} \tag{2}$$

A4.1.4 The Case

We use reciprocity and conservation of energy to compute the view factors for the case [39].

Table 13. Areas for the Package.

Surface	Area [m^2]
Upper Surface, A_{t2}	3.543×10^{-2}
Lower Surface, A_{b2}	1.110×10^{-1}
Side Surface, A_{s2}	3.854×10^{-1}
Total Surface, A_2	5.319×10^{-1}

Note: The upper surface is the one closest to the apex of the case. The lower surface is the one closest to the base of the case.

Using reciprocity, the view factor for the package from the case is

$$F_{1-2} = F_{2-1}A_2/A_1 = 6.665\times10^{-1}$$

where A_2 is the total surface area of the package and A_1 is the total interior surface area of the case.

Using reciprocity, the view factor for the AF&F from the case is

$$F_{1-3} = F_{3-1}A_3/A_1 = 1.514\times10^{-1}$$

where A_3 is the total surface area of the AF&F and A_1 is the total interior surface area of the case.

Using reciprocity, the view factor for the safety device from the case is

$$F_{1-4} = F_{4-1}A_4/A_1 = 4.143\times10^{-2}$$

where A_4 is the total surface area of the safety device and A_1 is the total interior surface area of the case.

Then by conservation of energy,

$$F_{1-1} = 1 - \sum_{i=2}^{4} F_{1-i} = 1.407\times10^{-1}$$

A4.2 Calculation of Exact View Factors

Michael F. Young calculated more exact values for the view factors under the assumptions that

Table 14. Module View Factors in the Test System.

From To	Case (1)	Package (2)	AF&F (3)	Safety Device (4)
Case (1)	1.407×10^{-1}	9.603×10^{-1}	8.036×10^{-1}	8.144×10^{-1}
Package (2)	6.665×10^{-1}	0.0	1.463×10^{-1}	0.0
AF&F (3)	1.514×10^{-1}	3.792×10^{-2}	0.0	1.856×10^{-1}
Safety Device (4)	4.143×10^{-2}	0.0	5.011×10^{-2}	0.0

Table 15. More Exact Module View Factors in the Test System.

From To	Case (1)	Package (2)	AF&F (3)	Safety Device (4)
Case (1)	1.66×10^{-1}	9.66×10^{-1}	7.86×10^{-1}	8.23×10^{-1}
Package (2)	6.70×10^{-1}	0.0	1.49×10^{-1}	0.0
AF&F (3)	1.23×10^{-1}	3.4×10^{-2}	0.0	1.77×10^{-1}
Safety Device (4)	4.10×10^{-2}	0.0	5.6×10^{-2}	0.0

1. Each body receives thermal radiation only from adjacent bodies. Thus $F_{2-4} = F_{4-2} = 0$.

2. All the thermal energy leaving the sides of each internal body reaches only the aeroshell.

Results of the calculations (which are described in [44]) are given in Table 15.

Appendix 5: Radiative Heat Transfer Equations for the Zero-Dimensional Models

The equations for the lumped-parameter thermal models given in the previous report describing the *Entero* code package [6] are incorrect; the corrected versions are presented here.

The lumped parameter models used in the *Entero* prototype consider only radiative and convective heat transfer and are formulated based on a simple energy balance assuming that each module has a single temperature.

Consider a system consisting of N modules, a case that encloses $N-1$ modules that is exposed to thermal radiation from the environment at a temperature T_0. All the surfaces are considered to be black surfaces. Therefore the emissivity, ε, is 1 for all surfaces, all the energy incident on a surface is absorbed by it, and there is no reflected thermal energy.

Let the environment be denoted by subscript 0, and the case by subscript 1. For each module k, the rate of change of its internal energy is the difference between the incident radiation (Q_i) and emitted radiation (Q_e), and the net convective heat transfer (Q_c)[2]

$$\frac{dE_k}{dt} = Q_{i,k} - Q_{e,k} + Q_{c,k}, \;\; k = 1, \ldots, N.$$

For a module k inside the case, the thermal radiation emitted by the module is

$$Q_{e,k} = \sigma T_k^4 A_k.$$

T_k is the absolute temperature of module k, σ is the Stefan-Boltzmann constant, and A_k is the area of surface k.

The thermal radiation incident on the module from another module j is

$$\begin{aligned} Q_{i,j\to k} &= \sigma T_j^4 F_{j\to k} A_j \\ &= \sigma T_j^4 F_{k\to j} A_k \end{aligned}$$

$F_{k\to j}$ is the view factor of surface k with respect to j.

The latter equality follows from reciprocity:

$$F_{j\to k} A_j = F_{k\to j} A_k.$$

[2] We use the convention that heat transfer into a body is positive.

Thus the total thermal radiation incident on module k from the other modules is

$$\begin{aligned} Q_{i,k} &= \sum_{j=1,\ j\neq k}^{N} Q_{i,j\to k} \\ &= \sigma A_k \sum_{j=1,\ j\neq k}^{N} F_{k\to j} T_j^4 \end{aligned}$$

Thus for the modules within the case,

$$\begin{aligned} \frac{dE_k}{dt} &= \sigma A_k \sum_{j=1,\ j\neq k}^{N} \left(F_{k\to j} T_j^4 - F_{k\to j} T_k^4\right) + Q_{c,k} \\ &= \sigma A_k \sum_{j=1}^{N} F_{k\to j} \left(T_j^4 - T_k^4\right) + Q_{c,k}, \quad k = 2,\ldots,N. \end{aligned}$$

where $A_1 = A_{1,i}$ is the interior surface area of the case and $F_{k\to 1}$ is the view factor for module k and the interior of the case

Finally,

$$\rho_k c_{pk} V_k \frac{dT_k}{dt} = \sigma A_k \sum_{j=1}^{N} F_{k\to j} \left(T_j^4 - T_k^4\right) + Q_{c,k}, \quad k = 2,\ldots,N.$$

or

$$\frac{\rho_k c_{pk} V_k}{\sigma A_k} \frac{dT_k}{dt} = \sum_{j=1}^{N} F_{k\to j} \left(T_j^4 - T_k^4\right) + \frac{Q_{c,k}}{\sigma A_k}, \quad k = 2,\ldots,N.$$

where ρ_k is the mass density of module k, c_{pk} is its specific heat capacity at constant pressure, and V_k is its volume.

For the case, the rate of change of the internal energy is the sum of the thermal radiation incident from the environment ($Q_{i,0\to 1}$) and the internal modules ($\sum_{j=2}^{N} Q_{i,j\to 1}$), and the thermal radiation emitted by the case to the environment ($Q_{e,1\to 0}$) and to the enclosed modules ($\sum_{j=2}^{N} Q_{i,1\to j}$), plus the net convective heat transfer:

$$\frac{dE_1}{dt} = Q_{i,0\to 1} + Q_{e,1\to 0} + \sum_{k=2}^{N} Q_{i,j\to 1} + \sum_{j=2}^{N} Q_{e,1\to j} + Q_{c,1}, \quad k = 1,\ldots,N. \tag{3}$$

From above we have

$$\begin{aligned} Q_{i,0\to 1} &= \sigma A_{1,o} F_{1\to 0} T_0^4 \\ Q_{e,1\to 0} &= -\sigma A_{1,o} F_{1\to 0} T_1^4 \\ \sum_{j=2}^{N} Q_{i,j\to 1} &= \sigma \sum_{j=2}^{N} A_j F_{j\to 1} T_j^4 \\ \sum_{j=2}^{N} Q_{e,1\to j} &= -\sigma \sum_{j=2}^{N} A_{1,i} F_{1\to j} T_1^4 \end{aligned}$$

where $A_{1,o}$ is the exterior surface area of the case. By reciprocity, the expression for $\sum_{j=2}^{N} Q_{i,j\to 1}$ can be written as

$$\sum_{j=2}^{N} Q_{i,j\to 1} = \sigma A_{i,1} \sum_{j=2}^{N} F_{1\to j} T_j^4$$

Substituting into Equation 3,

$$\begin{aligned} \frac{dE_1}{dt} &= \sigma A_{1,0} F_{1\to 0} T_0^4 - \sigma A_{1,0} F_{1\to 0} T_1^4 \\ &\quad + \sigma A_{i,1} \sum_{j=2}^{N} F_{1\to j} T_j^4 - \sigma \sum_{j=2}^{N} A_{1,i} F_{1\to j} T_1^4 \\ &\quad + Q_{c,1} \end{aligned}$$

or

$$\frac{dE_1}{dt} = \sigma A_{1,0} F_{1\to 0} \left(T_0^4 - T_1^4\right) + \sigma A_{i,1} \sum_{j=1}^{N} F_{1\to j} \left(T_j^4 - T_1^4\right) + Q_{c,1}$$

where the lower limit in the sum can be changed to "1" because the temperature difference will be zero when j equals 1.

Hence the rate of change of the internal energy of the case is given by (using Equation 4)

$$\rho_1 c_{p1} V_1 \frac{dT_1}{dt} = \sigma A_{1,o} F_{1\to 0} \left(T_0^4 - T_1^4\right) + \sigma A_{1,i} \sum_{j=1}^{N} F_{1\to j} \left(T_j^4 - T_1^4\right) + Q_{c,1}.$$

Or, rearranging,

$$\begin{aligned} \frac{\rho_1 c_{p1} V_1}{\sigma A_{1,o}} \frac{dT_1}{dt} &= F_{1\to 0} \left(T_0^4 - T_1^4\right) \\ &\quad + \frac{A_{1,i}}{A_{1,o}} \sum_{j=1}^{N} F_{1\to j} \left(T_j^4 - T_1^4\right) + \frac{Q_{c,1}}{\sigma A_{1,o}}. \end{aligned}$$

Consider next the convective heat transfer. In the prototype version of the *Entero* code package we included only convective heat transfer within the case; convective heat transfer to the environment was ignored. The convective heat transfer term $Q_{c,k}$ is given by

$$Q_{c,k} = \sum_{j=1}^{N} h_{k,j} A_{k,j} \left(T_j - T_k\right)$$

where $A_{k,j}$ is the area of module k that is convectively connected to module j, and $h_{k,j}$ is the convective heat transfer coefficient for this convective connection. As before, T_j is the temperature of module j. (Again note that heat transfer into a module is positive.)

Consistent with the lumped parameter models, we use empirical correlations for convective heat transfer. We assume that the convective fluid is dry air at normal temperature and pressure. The definitions for the terms in the correlations are given in Table 16. The convective heat transfer coefficients can be estimated from the correlations.

For a vertical, rectangular cavity with height H and a separation L between the heated surfaces, the Nusselt number, $\overline{Nu}_L$, can be correlated to the Rayleigh number, $\overline{Ra}_L$. Several correlations are available; one by Geankoplis [38, p. 452] is

$$\begin{aligned}
\overline{Nu}_L &= 0.22\left(\frac{Pr}{0.2+Pr}\overline{Ra}_L\right)^{0.28}(H/L)^{-1/4} \\
&\quad 2 < H/L < 10,\ Pr < 10^5,\ \overline{Ra}_L < 10^{10} \\
\overline{Nu}_L &= 0.18\left(\frac{Pr}{0.2+Pr}\overline{Ra}_L\right)^{0.29} \\
&\quad 1 < H/L < 2, 10^{-3} < Pr < 10^5, 10^3 < \left(\overline{Ra}_L Pr\right)/(0.2+Pr)
\end{aligned}$$

Another correlation, by MacGregor and Emery [38, p. 452], is

$$\begin{aligned}
\overline{Nu}_L &= 0.046\overline{Ra}_L^{1/3} \\
&\quad 1 < H/L < 40, 1 < Pr < 20, 10^6 < \overline{Ra}_L < 10^9
\end{aligned}$$

All properties are evaluated at the average temperature $(T_1+T_2)/2$, where T_1 and T_2 are the temperatures of the heated surfaces. More complex correlations are required for non-vertical cavities, but rather than use more sophisticated correlations, estimates for the convective heat transfer coefficient were made using typical temperatures of hydrocarbon and propellant fires and the MacGregor and Emery correlation (Equation 4). The estimates were 2.75–4.44 W/m^2-K; a value of 3.5 W/m^2-K was used as the default value for the convective heat transfer coefficient whenever convection was specified. (This value can be changed by the user).

Finally,

$$\begin{aligned}
\frac{\rho_1 c_{p1} V_1}{\sigma A_{1,o}}\frac{dT_1}{dt} &= F_{1\to 0}\left(T_0^4 - T_1^4\right) + \frac{A_{1,i}}{A_{1,o}}\sum_{j=1}^{N} F_{1\to j}\left(T_j^4 - T_1^4\right) \\
&\quad + \sum_{j=1}^{N}\frac{h_{1,j}A_{1,j}}{\sigma A_{1,o}}\left(T_j - T_1\right) \qquad (4)
\end{aligned}$$

Table 16. Definitions of Convective Heat Transfer Quantities

Symbol	Definition
$\overline{Nu}_L$	Average Nusselt number (based on length L) Ratio of convective heat transfer to conductive heat transfer $\overline{Nu}_L = \overline{h}L/k$
$\overline{h}$	Average convective heat transfer coefficient in the fluid
k	Thermal conductivity of the fluid
$\overline{Gr}_L$	Average Grashof number (based on length L) Ratio of the buoyancy forces to viscous forces $\overline{Gr}_L = \left[g\beta\left(T_s - T_0\right)L^3\right]/\nu^2$
g	Acceleration due to gravity
ν	Kinematic viscosity
μ	Dynamic viscosity
α	Thermal diffusivity, $\alpha = k/\left(\rho c_p\right)$
c_p	Specific heat at constant pressure
β	Thermal expansion coefficient
T_s	Surface temperature
T_0	Environment temperature
Pr	Prandtl number Ratio of molecular momentum and thermal diffusivities $Pr = c_p\mu/k = \nu/\alpha$
$\overline{Ra}_L$	Rayleigh number (based on length L) Ratio of buoyancy forces to thermal diffusivity $\overline{Ra}_L = \overline{Gr}_L Pr$

$$\frac{\rho_k c_{pk} V_k}{\sigma A_k} \frac{dT_k}{dt} = \sum_{j=1}^{N} F_{k \to j} \left(T_j^4 - T_k^4 \right) + \sum_{j=1}^{N} \frac{h_{k,j} A_{k,j}}{\sigma A_k} \left(T_j - T_k \right), \quad k = 2, \ldots, N. \tag{5}$$

Equations 4 and 5 provide the energy balances for lumped-parameter thermal radiation models for the case and enclosed modules, respectively. (Note that if the enclosed modules are themselves composed of other modules, the analysis for those modules must be modified.) These nonlinear ordinary differential equations can be solved using a variety of solvers, such as a Runge-Kutta solver.

Appendix 6: Tests of the Zero-Dimensional Algorithm

A6.1 Comparison to an Exact Solution

A simple test of the Runge-Kutta algorithm for the zero-dimensional models was conducted by setting the temperatures of all the modules except the AF&F to 1033 K and calculating the time required for the AF&F to reach a specified temperature.

Consider then the problem of calculating the temperature of a body with infinite thermal conductivity subject to thermal radiation from a constant temperature source that completely surrounds it. (This is the zero-dimensional model with a constant thermal radiation boundary condition.) This problem can be stated mathematically as

$$\rho c_p V \frac{dT}{dt} = \varepsilon\sigma A(T_0^4 - T^4) \quad (6)$$

$$T(0) = T_i \quad (7)$$

where $T(t)$ is the temperature of the body. ρ is the mass density of the body material, c_p is the specific heat capacity of the body material, V is the body volume, A is the surface area of the body, and ε is the emissivity of the body material. T_0 is the constant temperature of the environment, and σ is the Stefan-Boltzmann constant. ($\sigma = 5.6696 \times 10^{-8}$ W/m^2 – K^4.)

Equation 6 has the exact solution given by [45]

$$\tau = \frac{1}{2}\left[\frac{1}{2}\log\left(\frac{1+\hat{T}}{1-\hat{T}}\right) + \tan^{-1}(\hat{T})\right] + B \quad (8)$$

where $\hat{T} = T_1/T_s$, $\tau = t/t_s$, and B is an integration constant determined by the initial condition. t_s is a time scale given by

$$t_s = \frac{\rho c_p V}{A\varepsilon\sigma T_0^3} \quad (9)$$

Using values for ρ, c_p, and ε from Table 8 and for A and V from Table 5, Equation 8 provides the time required to reach a specified temperature. Exact and calculated times to reach temperatures from 400 K to 1000 K are given in Table 17, with relative errors.

A6.2 Test of the Convergence of the Zero-Dimensional Models with Time Step

The convergence of the zero-dimensional (lumped-parameter) models with the time step was tested. The default time step is 150.0 s. Time steps of 15.0 s and 1.5 s were also used. The results for the time steps of 150.0 s and 15.0 s are are shown in Figure 59.

Table 17. Solutions for the Thermal Radiation Heating Problem[a].

Temperature [K]	Exact Time[b] [s]	Calculated Time[c] [s]	Relative Error[d]
400	73.25	73.04	-2.87×10^{-3}
500	148.26	147.84	-2.83×10^{-3}
600	226.96	226.31	-2.86×10^{-3}
700	312.91	312.02	-2.84×10^{-3}
800	413.65	412.48	-2.83×10^{-3}
900	549.71	548.15	-2.84×10^{-3}
1000	838.73	836.35	-2.84×10^{-3}

[a] Material and geometric properties given in text; $T(0)$ = 300 K.
[b] Solution calculated with Equation 8.
[c] Solution calculated by the *Entero* integrator using the fourth-order Runge-Kutta algorithm (0.1 s time step).
[d] Relative error = $(T_c - T_e)/T_e$, where T_c and T_e are the calculated and exact solutions, respectively.

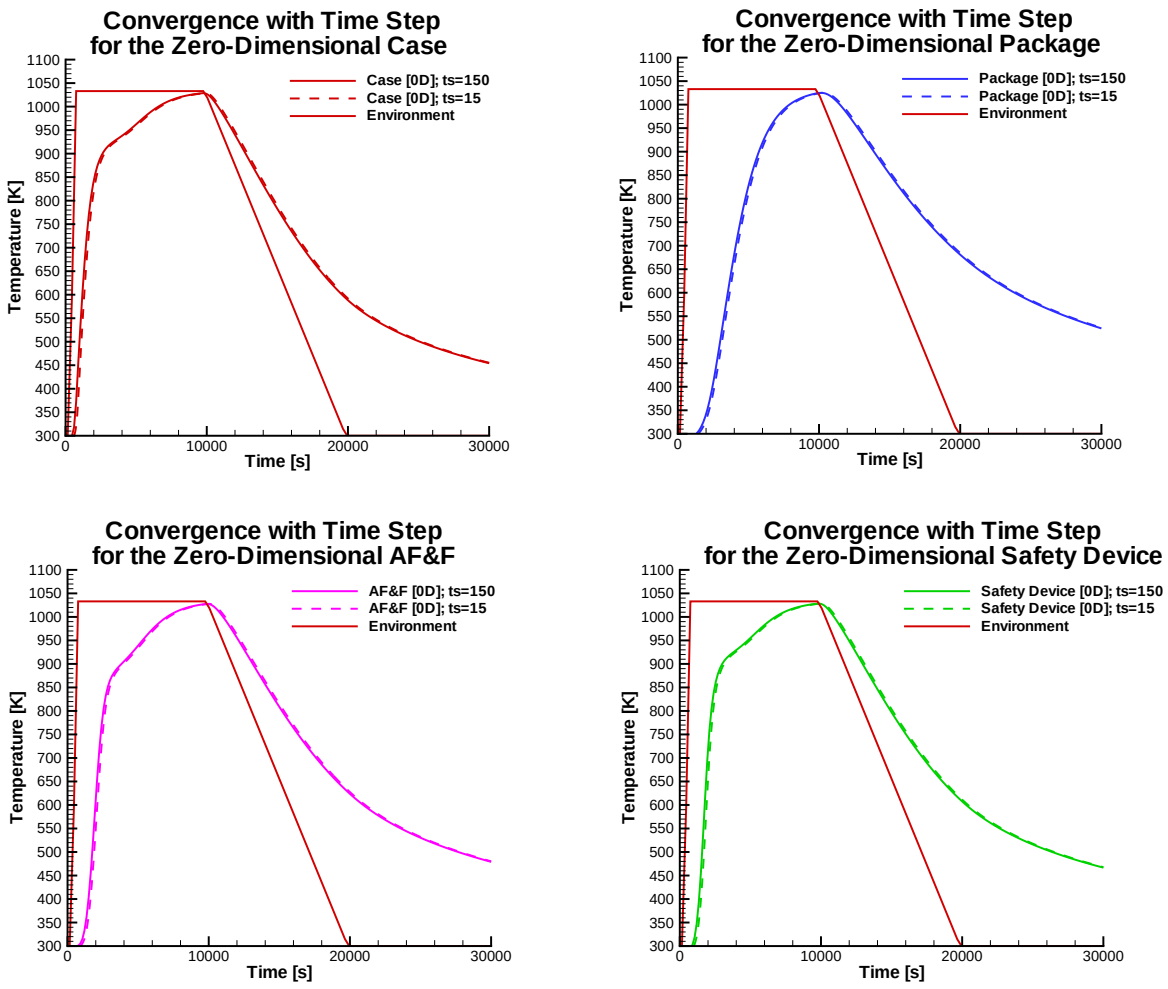

Figure 59. Convergence of the Zero-Dimensional Models with Time Step.

Table 18. Convergence of the Zero-Dimensional Models with Time Step.

Time Step [s]	150.0	15.0	1.50
Maximum Difference[a]	—	$\Delta_0 = 0.11$	$\Delta_1 = 0.012$

[a] Δ_i is defined in the text.

The differences are quantified in Table 18 for the AF&F. In this table, the maximum difference between adjacent solutions given. The maximum difference is calculated from the equation

$$\begin{aligned} \Delta_i &= \max_{t_n \in \tau_i} |T_i(t_n) - T_{i+1}(t_n)| / T_{i+1}(t_n) \\ \tau_i &= \{t : t = n\delta_i t, n = 0, \ldots, N_i\} \end{aligned}$$

where T_i is the temperature solution calculated with time step δ_i, $(\delta_0, \delta_1, \delta_3) = (150.0 \text{ s}, 15.0 \text{ s}, 1.50 \text{ s})$ and $(N_0, N_1, N_2) = (200, 2000, 20000)$

Appendix 7: Calculation of the Surface-Average Temperature

The surface-averaged temperature of a finite element mesh is given by

$$\overline{T}(t) = \frac{1}{A} \sum_{i \in S} T_i(t) \int_{A_i} \Phi_i(x,y,z) dA \tag{10}$$

where A is the total surface area of the mesh and A_i is the exposed element face on which Φ_i is supported.

Appendix 8: Calculation of the Volume-Average Temperature

The rate of change of the total energy E_t of a body composed of a single material with time is given by

$$\frac{dE_t}{dt} = \int_V \rho c_p \frac{dT}{dt} dV$$

where V is the volume of the body, ρ is the mass density, c_p is the heat capacity, T is the temperature, and t is the time. For a lumped-parameter model of the body,

$$\frac{dE_t}{dt} = \rho c_p V \frac{dT_l}{dt}$$

For a finite-element model of the body, the temperature in the body is given by

$$T(x,y,z,t) = \sum_i \Phi_i(x,y,z) T_i(t)$$

where (x,y,z) are the spatial coordinates, $T_i(t)$ is the temperature at a specified point (x_i,y_i,z_i) and $\Phi_i(x,y,z)$ is a shape function.

Thus for the finite-element model, the rate of total energy change is

$$\begin{aligned} \frac{dE_t}{dt} &= \int_V \sum_{i=1}^{N} \rho c_p \Phi_i(x,y,z) \frac{dT_i}{dt} dV \\ &= \rho c_p \sum_{i=1}^{N} \int_V \Phi_i(x,y,z) dV \frac{dT_i}{dt} \end{aligned}$$

Equating the rates predicted by the two models,

$$\rho c_p V \frac{dT_l}{dt} = \rho c_p \sum_{i=1}^{N} \int_V \Phi_i(x,y,z) dV \frac{dT_i}{dt}$$

or

$$\frac{dT_l}{dt} = \frac{1}{V} \sum_{i=1}^{N} \int_V \Phi_i(x,y,z) dV \frac{dT_i}{dt}$$

Therefore, the temperature predicted by the lumped parameter model should be compared to the average temperature given by

$$T_l = \frac{1}{V} \sum_{i=1}^{N} \int_V \Phi_i(x,y,z) dV T_i \tag{11}$$

Since T_i is independent of the spatial variables and in the problems considered here the mesh is fixed in space, the shape-function integrals can be computed independently.

References

[1] W. E. Vesely, F. F Goldberg, N. H Roberts, and D. F. Haasl. Fault Tree Handbook. Technical Report NUREG-0492, United States Nuclear Regulatory Commission, January 1981.

[2] ASCI Update. Sandia National Laboratories, Albuquerque, New Mexico, October 2000. `www.sandia.gov/ASCI/asciupdate/0010update.pdf`.

[3] E. R. Keiter, S. A. Hutchinson, R. J. Hoekstra, E. L. Rankin, T. V. Russo, and L. J. Waters. Computational algorithms for device-circuit coupling. Technical Report SAND2003-0080, Sandia National Laboratories, Albuquerque, NM, January 2003.

[4] D. R. Gardner, J. P. Castro, P. N. Demmie, M. A. Gonzales, G. L. Hennigan, M. F. Young, and Sudip S. Dosanjh. Developing a Flexible System Modeling Environment for Engineers. In *Proceedings of the 35th Hawaii International Conference on Systems Sciences*, Hilton Waikoloa Village, Big Island HI, 7–10 January 2002.

[5] D. R. Gardner, J. P. Castro, P. N. Demmie, M. A. Gonzales, G. L. Hennigan, and M. F. Young. The *Entero* Project: Developing a Multifidelity System Environment for Design Engineers. In *Proceedings of the Summer Computer Simulation Conference 2002*, San Diego, CA, 14–18 July 2002.

[6] D. R. Gardner, J. P. Castro, G. L. Hennigan, and B. H. Cole II. A Prototype of the *Entero* System Engineering Code Package. Technical Report SAND2000-1368, Sandia National Laboratories, Albuquerque, NM, June 2000.

[7] D. R. Gardner, J. P. Castro, M. A. Gonzales, G. L. Hennigan, and M. F. Young. On the Development of a Java-Based Tool for Multifidelity Modeling of Coupled Systems: LDRD Final Report. Technical Report SAND 2002-3783, Sandia National Laboratories, Albuquerque, NM, November 2002.

[8] P. K. Davis. Exploratory Analysis Enabled by Multiresolution, Multiperspective Modeling. In *Proceedings of the 2000 Winter Simulation Conference*, pages 293–302, Orlando, FL, 10–13 December 2000. IEEE.

[9] G. Follen and M. auBouchon. Numerical Zooming Between the NPSS Version 1 and a 1-Dimensional Meanline Design Analysis Code. In *Proceedings of the ISABE, the 14th International Symposium on Air Breathing Engines*, Florence, Italy, 5–10 September 1999. AIAA-99-7196.

[10] P. K. Davis and J. H. Bigelow. Experiments in Multiresolution Modeling (MRM). Technical Report MR-1004-DARPA, RAND, Santa Monica, CA, 1998.

[11] P. K. Davis. An Introduction to Variable-Resolution Modeling and Cross-Resolution Model Connection. In *Proceedings of the Conference on Variable-Resolution Modeling*, Washington, D.C., 5–6 May 1992. RAND Report CF-103-DARPA.

[12] Paul K. Davis. An Introduction to Variable-Resolution Modeling and Cross-Resolution Model Connection. Technical Report R-4252-DARPA, RAND, Santa Monica, CA, 1993.

[13] P. K. Davis and R. K. Huber. Variable-Resolution Combat Modeling: Motivations, Issues, and Principles. Technical Report N-3400-DARPA, RAND, Santa Monica, CA, 1992.

[14] D. R. Powell. Control of Entity Interactions in Hierarchical Variable Resolution Simulation. Technical Report LA-UR-97-1287, Los Alamos National Laboratory, Los Alamos, NM, 1997.

[15] K. W. Brendley and J. Marti. A Distributed Network Approach to Variable Resolution Modeling. In *Proceedings of the Conference on Variable-Resolution Modeling*.

[16] P. F. Reynolds, Jr., S. Srinivasan, and A. Natrajan. Consistency Maintenance in Multi-Resolution Simulations. *ACM Transactions on Modeling and Simulations*, 7(3):368–392, July 1997.

[17] Paul K. Davis and Richard Hillestad. Families of Models that Cross Levels of Resolution: Issues for Design, Calibration, and Management. In *Proceedings of the 1993 Winter Simulation Conference*.

[18] P. K. Davis and J. Bigelow. Introduction to Multi-Resolution Modeling (MRM) with an Example Involving Precision Fires. In *Proceedings of the Enabling Technology for Simulation Science II Conference*, pages 14–27, Orlando, FL, April 1998. SPIE.

[19] R. Radhakrishnan and P. A. Wilsey. Ruminations on the Implications of Multi-Resolution Modeling on DIS/HLA. In *Proceedings of the 3rd IEEE International Workshop on Distributed Interactive Simulation and Real-Time Applications*.

[20] A. Natrajan and A. Nguyen-Tuong. To Disaggregate or Not to Disaggregate, That Is *Not* the Question. In *Proceedings of the Electronic Conference on Scalability in Training Simulation (ELECSIM '95)*, CS-95-18. Society for Computer Simulation, 10 April–18 June 1995.

[21] A. Natrajan, P. F. Reynolds, and Sudhir Srinivasan. MRE: An Approach to Multi-Resolution Modeling. In *Proceedings of PADS'97*, Lockenhaus, Austria, 10–13 July 1997.

[22] R. J. Hillestad and M. L. Juncosa. Cutting Down Some Trees to See the Forest: On Aggregation and Disaggregation in Combat Models. In *Proceedings of the Conference on Variable-Resolution Modeling*, pages 256–292, Washington, D.C., 5–6 May 1992. RAND Report CF-103-DARPA.

[23] Bruce W. Fowler. Resolution Changes and Renormalization for Partial Differential Equation Combat Models. In *Proceedings of the Conference on Variable-Resolution Modeling*.

[24] A. F. Sisti and S. D. Farr. Model Abstraction Techniques: An Intuitive Overview. In *Proceedings of the National Aerospace Electronics Conference*, Dayton, OH, July 1998.

[25] A. F. Sisti and S. D. Farr. Modeling and Simulation Enabling Technologies for Military Applications. In *Proceedings of the Winter Computer Simulation Conference*, Coronado, CA, December 1996.

[26] D. Caughlin and A. F. Sisti. A Summary of Model Abstraction Techniques. In *Proceedings of the Enabling Technology for Simulation Science I Conference*, pages 2–13, Orlando, FL, April 1997.

[27] K. Lee and P. A. Fishwick. Dynamic Model Abstraction. In *Proceedings of the 1996 Winter Simulation Conference*, Coronado, CA, 8–11 December 1996. Society for Computer Simulation.

[28] F. K. Frantz. Analyzing Models for Abstraction. In *Proceedings of the Enabling Technology for Simulation Science I Conference*, pages 14–21, Orlando, FL, April 1997. SPIE.

[29] F. K. Frantz. A Taxonomy of Model Abstraction Techniques. Technical Report RL-TR-96-87, Air Force Rome Laboratory, Rome, NY, August 1996.

[30] A. T. Norris. Automated Simplification of Full Chemical Mechanisms: Implementation in the National Combustion Code. In *Proceedings of the 34th AIAA/ASME/SAE/ASEE Joint Propulsion Conference & Exhibit*, Cleveland, OH, 13–15 July 1998. AIAA 98-3987.

[31] L. Acar, J. S. Albus, and A. M. Meystel. A Mathematical Representation of Multiresolutional World Modeling. In *Proceedings of the 1995 IEEE International Symposium on Intelligent Control*, Monterey, CA, 27–29 August 1995. The Institute of Electrical and Electronics Engineers (IEEE).

[32] J. A. Reed and A. A. Afjeh. Connecting Components of Varying Fidelity in a Turbofan Engine Simulation. *Modeling and Simulation—Control, Signal Processing, Robotics, Power*, 23(4):2291–2298, 1992.

[33] J. A. Reed and A. A. Afjeh. Integrating Computer Generated Fan Performance Data with a Turbofan Engine Simulator. In *Proceedings of the Modelling, Simulation, and Identification Conference*, pages 83–90, Vancouver, BC, August 1992.

[34] J. A. Reed and A. A. Afjeh. A Comparative Study of High and Low Fidelity Fan Models for Turbofan Engine System Simulation. In *Proceedings of the IASTED International Conference on Applied Modelling and Simulation*, Banff, Canada, July 1997.

[35] P. J. Roach. *Computational Fluid Dynamics*. Hermosa Publishing Company, Albuquerque, NM, 1985.

[36] P. F. Chavez. On the L_2-Projection for Transferring Data Between Finite Element Meshes. In *5th International Symposium on Finite Elements and Flow Problems*, pages 509–514, 23–26 January 1984.

[37] D. K. Gartling and R. E. Hogan. Coyote–A Finite Element Computer Program for Nonlinear Heat Conduction Problems. Part I–Theoretical Background. Version 3.03. Technical Report SAND94-1173, Sandia National Laboratories, Albuquerque, NM, December 1999.

[38] F. P. Incropera and D. P. DeWitt. *Fundamentals of Heat Transfer*. John Wiley & Sons, New York, NY, 1981. Tables A.1–A.4.

[39] R. Siegel and J. R. Howell. *Thermal Radiation Heat Transfer*. Hemisphere Publishing Corporation, Washington, D.C., second edition, 1981.

[40] D. K. Gartling, R. E. Hogan, and M. W. Glass. Coyote–A Finite Element Computer Program for Nonlinear Heat Conduction Problems. Part II–User's Manual. Version 3.03. Technical Report SAND94-1173, Sandia National Laboratories, Albuquerque, NM, December 1999.

[41] A. Geist, A. Beguelin, J. Dongarra, W. Jiang, R. Manchek, and V. Sunderam. *PVM: Parallel Virtual Machine—A Users' Guide and Tutorial for Networked Parallel Computing*. MIT Press, Cambridge, MA, 1994.

[42] The Spice Circuit Simulator Home Page. `infopad.eecs.berkeley.edu:80/~icdesign/SPICE`.

[43] S. Hutchinson, E. Keiter, R. Hoekstra, H. Watts, A. Waters, T. Russo, R. Schells, and C. Bogdan. The Xyce™ Parallel Electronic Simulator–An Overview. In *Proceedings of Parallel Computing 2001 (ParCo2001)*, Naples, Italy, 4–7 September 2001.

[44] M. F. Young. Comparison of View Factors for *Entero* Phase II Test Problem, 22 October 2001.

[45] R. C. Weast, editor. *CRC Handbook of Chemistry and Physics*. CRC Press, Cleveland, OH, 55th edition, 1974. p. A-119.

Distribution

1	MS 0321	W. J. Camp, 9200
1	0847	S. A. Mitchell, 9211
1	0310	M. D. Rintoul, 9212
1	1110	D. E. Womble, 9214
1	1111	B. A. Hendrickson, 9215
1	0310	R. W. Leland, 9220
1	0316	P. Yarrington, 9230
1	0819	E. A. Boucheron, 9231
1	0819	P. F. Chavez, 9232
1	0316	S. S. Dosanjh, 9233
1	0316	J. P. Castro, 9233
16	0316	D. R. Gardner, 9233
10	0316	G. L. Hennigan, 9233
1	0316	R. J. Hoekstra, 9233
1	0316	S. A. Hutchinson, 9233
1	0316	E. R. Keiter, 9233
1	0316	C. C. Ober, 9233
1	0316	R. C. Schmidt, 9233
1	0316	J. N. Shadid, 9233
1	0316	J. B. Aidun, 9235
1	1137	M. A. Gonzales, 6535
1	0739	M. F. Young, 6415

1	MS 9018	Central Technical Files, 8945-1
2	0899	Technical Library, 9616
1	0612	Review & Approval Desk, 9612 for DOE/OSTI